

Ka-Band Dual Copolarized Empirical Model for the Sea Surface Radar Cross Section

Yury Yu Yurovsky, Vladimir N. Kudryavtsev, Semyon A. Grodsky, and Bertrand Chapron

Abstract—This paper presents dual copolarized (PP) (VV and HH) Ka-band sea surface backscattering measurements taken from the Black Sea research platform at incidence angles ranging from 25° to 65° and in the wind speed range from 3 to 18 m/s. These measurements are corrected for radar antenna pattern and geometry of observations. The resulting normalized radar cross section (NRCS) is parameterized in a form of truncated azimuthal Fourier series with coefficients dependent on the incidence angle and wind speed. This dual PP empirical model (KaDPMoD) is consistent with the Ku-band NSCAT-4 model. However, some remarkable differences are revealed. They are apparent when analyzed using a decomposition of VV and HH measurements into polarized Bragg backscattering (polarization difference, $PD = VV - HH$) and nonpolarized (NP) backscattering from breaking waves. The polarization difference (PD) has strong azimuth and wind dependencies, with the wind exponent ranging from 2.5 to 3. The saturation wave spectra derived from multifrequency PD (based on KaDPMoD and Ku- and C-band empirical models) have a notable peak in the capillary-gravity range. The relative contribution of NP radar return to the Ka-band NRCS is significant. In the upwind direction, it reaches up to 60%–80% and 25%–50% for HH and VV, respectively. It is found that the NP wind exponent is lower than that for Bragg backscattering. Therefore, the relative contribution of the NP to Ka-band NRCS decreases with increasing wind speed at both polarizations. Such a behavior is the opposite of that observed in the Ku-band.

Index Terms—Capillary waves, cross section, radar backscattering, sea surface, wave breaking.

I. INTRODUCTION

ACTIVE microwave sensors are powerful tools for the ocean remote sensing. Most of them operate in decimeter or centimeter radio bands (L-, C-, X-, and Ku-band) and have

Manuscript received March 22, 2016; revised May 31, 2016, August 1, 2016, and September 23, 2016; accepted October 21, 2016. The work was supported by the Russian Science Foundation under Grant 15-17-20020. The work of S. Grodsky was supported by NASA/Physical Oceanography under Grant NNX15AG40G.

Y. Y. Yurovsky is with the Federal State Budget Scientific Institution, Marine Hydrophysical Institute of RAS, Sevastopol 299011, Russia (e-mail: yyyurovsky@gmail.com).

V. N. Kudryavtsev is with the Federal State Budget Scientific Institution, Marine Hydrophysical Institute of RAS, Sevastopol 299011, Russia, and also with the Satellite Oceanography Laboratory, Russian State Hydrometeorological University, Saint Petersburg 195196, Russia (e-mail: kudr@rshu.ru).

S. A. Grodsky is with the Department of Atmospheric and Oceanic Science, University of Maryland at College Park, College Park, MD 20742 USA (e-mail: senya@umd.edu).

B. Chapron is with the Institut Français de Recherche pour l'Exploitation de la Mer, 29280 Plouzané, France (e-mail: bertrand.chapron@ifremer.fr).

Color versions of one or more of the figures in this paper are available online at <http://ieeexplore.ieee.org>.

Digital Object Identifier 10.1109/TGRS.2016.2628640

typical ground footprints of the order of tens kilometers (for real aperture sensors). A demand for higher spatial resolution and detection of coastal phenomena requires exploration of higher radar frequencies, which is also expected to improve surface topography accuracy. The first spaceborne Ka-band (35.75 GHz) altimeter, AltiKa [1], launched in 2013, has demonstrated almost a factor of three improvement in sea level retrieval accuracy in comparison with the previous Ku-band TOPEX/Poseidon. The launch of a new Ka-band interferometer, KaRIN, designed for the Surface Water Ocean Topography mission, scheduled for 2019, is expected to provide the first radar mesoscale ocean survey [2]. Atmospheric attenuation, which becomes increasingly important in millimeter radio bands, needs to be accounted for in ocean applications. On the other hand, measurements in this band provide information on the atmospheric state, and are used for rainfall retrieval by the Global Precipitation Measurement mission dual-frequency Ku-/Ka-band radar [3].

It is expected that future ocean applications of millimeter-range radars will combine their higher spatial resolution with synthetic aperture radar (SAR) capabilities [4]–[6]. In fact, Ka-band airborne SAR instruments have already demonstrated incredible spatial resolution of down to 10 cm, significantly exceeding the resolution of traditional C- and X-band instruments [7].

Besides various applications based on detection of backscattering intensity, radar Doppler frequency spectra can provide direct measurements of the line-of-sight projection of surface currents over the global ocean [8], [9]. The conical rotating Doppler scatterometer configuration enables instruments of this type to retrieve surface current velocity, while the use of the higher Ka-band frequency should increase the spatial resolution and retrieval accuracy by a factor of three [10].

Development and understanding of Ka-band capabilities require accurate characterization of geophysical model functions (GMFs) relating the sea surface cross section and the Doppler frequency shift as a function of environmental variables and the observation geometry. To date, the most well-established GMFs are developed for the lower radar frequencies, e.g., C-band CMOD5.N [11], Ku-band QSCAT-1 [12], and NSCAT [13], [14].

Ka-band measurements for various observation geometries are still quite rare. A complete tabulated model for VV and HH polarizations has been proposed in [15] (hereinafter referred to as MOSN'86). That table was based on airborne measurements in a wide range of incidence angles (from 0° to 70°) and wind speeds (from 3.2 to 17.2 m/s). A corresponding MOSN'86

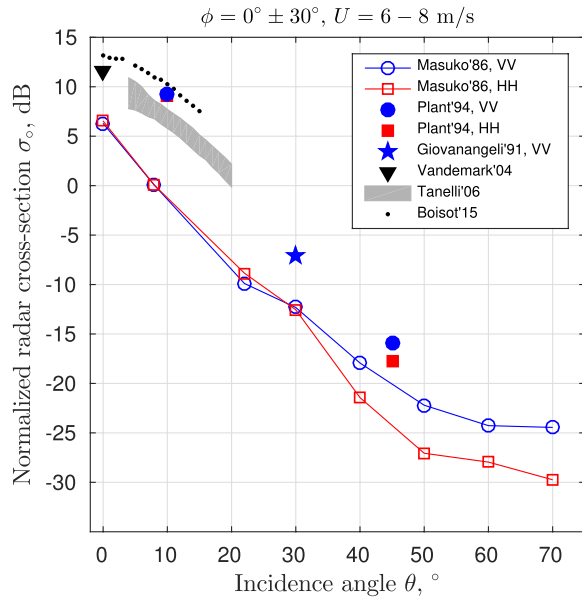


Fig. 1. Ka-band upwind NRCS versus incidence angle at 6–8-m/s wind speed. Blue line, dot, and asterisk: VV polarization. Red line and square: HH polarization. Black dots and inverted triangle: unknown (no matter) polarization. Data sources are listed by the first author and publication year.

analytical parametrization [16] is available only for VV polarization and only for fixed incidence angles of 30°, 40°, 50°, and 60°.

However, a number of independent measurements show significant deviations from MOSN’86 (Fig. 1). In particular, a notable positive deviation of about 5–6 dB [17]–[19] at near-nadir angles has been observed, which has been attributed to uncertainties in the absolute calibration. The absolute calibration was made in [15] separately for transmitter and receiver, but not for the entire system. At moderate incidence angles, both field data [20] and wind-wave tank data [21], [22] show backscattering levels exceeding those described in MOSN’86.

Ka-band backscattering data are thus not numerous and those that do exist demonstrate significant scatter. This paper aims to narrow this scatter using Ka-band Doppler dual copolarized (PP) (VV and HH) data collected during a number of field experiments carried out from the Black Sea research platform during 2009–2015. Observed features of Ka-band backscattering are discussed and compared with independent Ka- and Ku-band radar measurements.

II. EXPERIMENT

A. Equipment

The measurements are taken from a research platform operated by Marine Hydrophysical Institute, which is located in the Black Sea 600 offshore of Katsiveli (44°23’35” N, 33°59’04” E) in a 25- to 30-m deep water (Fig. 2).

The experiments were carried out using Ka-band (37.5 GHz, 8-mm wavelength) continuous-wave Doppler radar. The radar has two conical horn antennas for transmitting and receiving. Antenna horn axes are parallel and separated by 35 cm. The length of the horn axis is 38 cm and the diameter of the aperture is 16.5 cm. The polarization

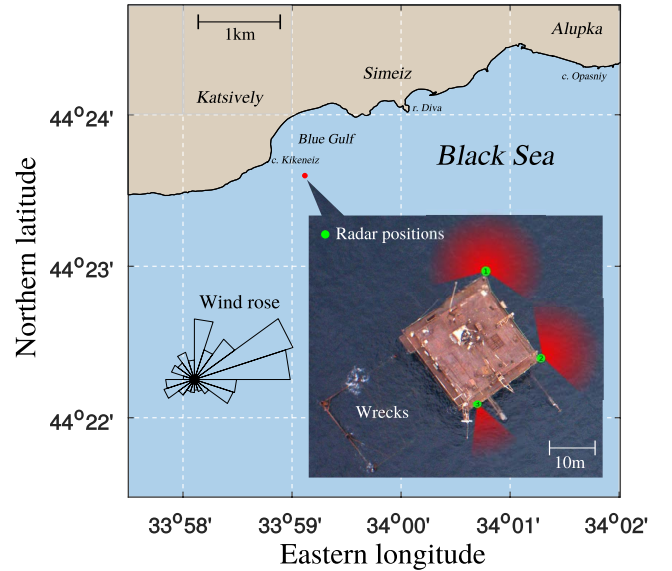


Fig. 2. Black Sea Research platform site and top view. Radar positions are marked by the green circles, possible azimuths at each position are shown by the red sectors. Wind rose is plotted for the boreal autumn. “Wrecks” indicate the location of the platform module destroyed by storms.

plane of the Gunn-diode-based transmitter is rotated by 45° from the radar incidence plane so that vertical and horizontal components are radiated simultaneously. The receiver has two separate vertical and horizontal channels. Such a hybrid radar design does not allow discrimination between PP and cross-polarized (CP) signals. In fact, vertical and horizontal channels receive a mixture of VV+HV and HH+VH components, respectively. However, at wind speeds below 25 m/s, the CP signal is much lower than the PP (VV and HH) signals [23]–[25]. Hence, we ignore the CP contribution and consider the hybrid vertical and horizontal signals as “pure” PP, VV and HH, signals (see Appendix B for more discussions).

The radar has a built-in high-pass filter with a 5-Hz cutoff frequency to avoid reflections from static objects. In-phase and quadrature channels for each polarization are digitized at 40 kHz using a PC-based 14-b analog-to-digital converter.

Wind speed and direction are measured using a standard cup anemometer and wind vane installed on top of the platform mast at 21 m above the sea surface. The air temperature, pressure, and humidity at a 21-m height and water temperature at a 3-m depth are continuously monitored by a commercial weather station (Davis Vantage Pro2 6152). Supplementary wave information is obtained using a wire wave gauge installed from an 11-m-long horizontal boom. The neutral wind speed at 10 m, U , is computed from the meteorological observations and near-surface water temperature using the COARE3.0 algorithm [26].

B. NRCS Measurement

A few metal targets (trihedral corner reflectors and spheres of different sizes) were used to calibrate the radar and estimate its two-way patterns (see Appendix A). The radar beam width is not symmetrical and is wider in the polarization

plane (15° at -3 dB; see Fig. 18). The calibration was repeatedly performed during each field campaign, but no significant changes were detected.

The backscattered power p' from a stand-alone point-like reference target is determined by the radar equation

$$p' = C \frac{\Gamma'}{R'^4} \sigma' \quad (1)$$

where C is the calibration constant determined by the radar architecture (see Appendix A), Γ' is the two-way radar pattern in the direction of the target, R' is the distance to the target, and σ' is the radar cross section (RCS) of the target.

Because the sea surface is a distributed target, its radar backscattering is integrated over the antenna pattern

$$p = \frac{C}{R_0^4} \int \Gamma_{\text{eff}}(x, y) \sigma_o dx dy = \frac{C}{R_0^4} \sigma_{\text{eff}} \quad (2)$$

where $\sigma_o(x, y)$ is the sea surface normalized RCS (NRCS) that varies spatially depending on the sea surface $\{x, y\}$ -coordinates, $\Gamma(x, y)$ is the two-way radar angular pattern in the direction of $\{x, y\}$ -point on the surface, $R(x, y)$ is the slant range to the $\{x, y\}$ -point, R_0 is the slant range along the radar principal axis, $\Gamma_{\text{eff}}(x, y) = \Gamma(x, y)(R_0/R(x, y))^4$ is the effective pattern accounting for changes in the slant range, and σ_{eff} is the effective RCS of the spatially distributed sea surface target.

For an infinitely narrow radar angular pattern, σ_o is almost constant within the radar surface footprint and can be taken out the integral in (2). However, in our case, the radar angular pattern is notably wide, and thus the parameter we measure is a convolution of $\sigma_o(x, y)$ and $\Gamma(x, y)$. Because the NRCS dependence on the incidence angle is much stronger than the dependence on the azimuth angle, the antenna pattern impact is stronger for VV than for HH polarization.

The effective (measured) NRCS of the distributed sea surface target is defined as the ratio of effective RCS σ_{eff} and effective radar footprint, $\mathcal{S}_{\text{eff}} = \int \Gamma_{\text{eff}}(x, y) dx dy$, and reads

$$\sigma_{\text{oeff}} = \frac{\sigma_{\text{eff}}}{\mathcal{S}_{\text{eff}}} = p \frac{R_0^4}{C} \left[\int \Gamma(x, y) \left(\frac{R_0}{R(x, y)} \right)^4 dx dy \right]^{-1}. \quad (3)$$

Radar internal noise prevents measurements at calm winds and/or high incidence angles. Its level (estimated from clear sky radar backscattering) is subtracted from the measured radar backscattering. Radar data are disregarded if their signal-to-noise ratio is below 1. The noise level of NRCS is estimated from (3) by substituting the received power by its noise variance (Fig. 3). Discontinuity of the NRCS noise curves in Fig. 3 at $\theta = 45^\circ$ is related to different altitudes used for the radar measurement at $\theta < 45^\circ$ and $\theta > 45^\circ$. The noise level determines the critical incidence angles and winds for which radar backscattering from the sea surface is detectable. In our observations, the signal-to-noise ratio falls below one at $\theta > 70^\circ$ for HH polarization at winds below 5–6 m/s. Thus, the upper limit of θ for our data is set to 70° .

C. Data Set

The radar look direction and the start of the acquisition cycle were chosen manually depending on wind and

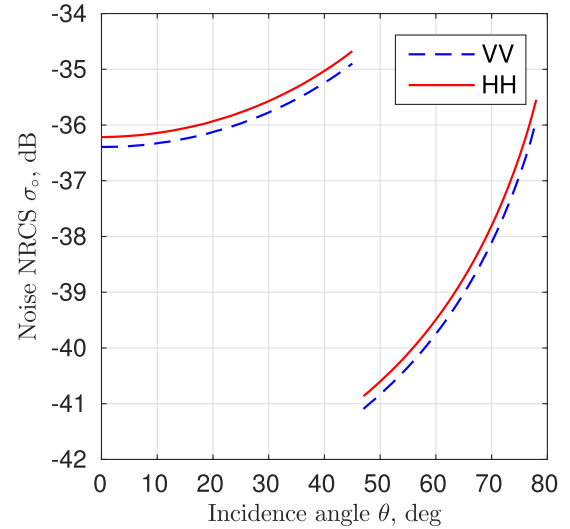


Fig. 3. Noise level of the measured NRCS as a function of the incidence angle. The discontinuity at $\theta = 45^\circ$ is caused by the difference in radar heights at a different θ .

wave conditions. Typical records last from from 5 to 60 min. For the processing purposes, each record was split into 5-min fragments, which we refer to as data samples. The total number of data samples is about 1500.

Depending on the incidence angle θ , the radar is installed on the top or bottom deck of the platform. The top deck installation (13.5-m height) is used for incidence angles $0^\circ \leq \theta \leq 45^\circ$, while the bottom installation (6.5-m height) is used for higher incidence angles, $\theta > 45^\circ$. In both cases, the far-field approximation is applicable.

Assuming that the NRCS is symmetrical relative to the wind direction, the data are folded in the azimuth range, $0^\circ \leq \phi \leq 180^\circ$. To minimize the impact of platform-induced wind distortions on downwind measurements, all downwind observations were carried out from the most outlying platform corner, so that the radar beam was never directed toward the platform “shadow” zone (Fig. 2).

Most of the data samples correspond to moderate ($45^\circ < \theta < 55^\circ$) and high ($\theta = 70^\circ$) incidence angles, while the near-nadir data ($\theta < 30^\circ$) are sparse [Fig. 4(a)].

The observed wind speed U varies from 3 to 18 m/s with the most common speeds falling in the range from 5 to 11 m/s [Fig. 4(c)]. There are three typical wind directions at the platform location: easterly, southwesterly, and northerly (Fig. 2). The latter is removed from the analysis because it corresponds to offshore winds and short (~ 1 km) wave fetches. For easterly or southwesterly winds, the wave fetch is determined by the size of atmospheric synoptic systems and can reach a few hundred kilometers. Our analysis avoids transient wind/wave conditions and focuses on temporally stable conditions typical of the open ocean. In addition, we also exclude the cases of the swell-dominated sea. Swell-induced strong radar backscattering modulations, which may significantly affect the mean radar signal, are out of the scope of this paper.

Fig. 5 illustrates an example of measured NRCS as a function of θ , ϕ , and U for cases with rather good statistics.

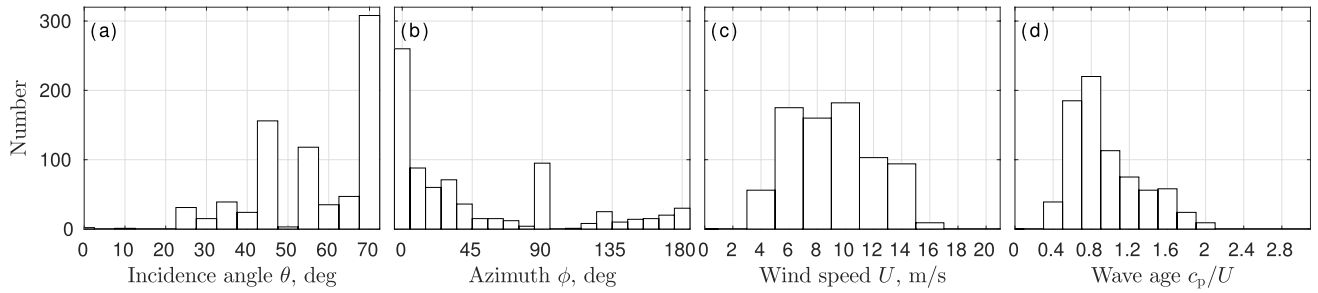


Fig. 4. Data set statistics. Distribution of measurements on (a) incidence angle, (b) radar versus wind azimuth (zero is upwind), (c) wind speed, and (d) wave age.

The antenna pattern impact on the measured NRCS is clearly seen at near-nadir θ , where σ_o for VV polarization is higher than that for HH polarization, while they must be the same for specular reflections dominating at low θ [Fig. 5(a)–(c)].

In contrast to the incidence angle dependence, the azimuth dependence of measured NRCS is not strongly affected by the antenna pattern and the “true” NRCS azimuthal features can be directly inferred from measured NRCS. At moderate incidence angles [$\theta = 45^\circ$; see Fig. 5(e)], the azimuth dependence of NRCS has expected characteristics with a minimum in the crosswind direction and local maxima in the upwind and downwind directions. At these angles, the upwind backscattering exceeds the downwind backscattering. At lower incidence angles [$\theta = 32^\circ$; see Fig. 5(d)], the upwind minus downwind NRCS difference vanishes (if not actually changes sign) demonstrating that backward wave slopes may be “rougher.” At high incidence angles [$\theta = 70^\circ$; see Fig. 5(f)], the azimuth distribution becomes unimodal, with a clear upwind maximum and a minimum in the downwind direction, which is even lower than the crosswind NRCS.

In general, wind dependencies of measured NRCS follow the power law, $\sigma_o \sim U^N$ [Fig. 5(g)–(i)]. However, some evidence of saturation is seen at rather strong winds, $U > 15$ m/s [Fig. 5(h)].

As already observed, the measured NRCS, especially for VV polarization, is significantly affected by the radar antenna pattern. Therefore, in order to infer the true NRCS, the measured NRCS must be corrected for the impact of the radar antenna pattern.

III. RESULTS

A. Data Fitting

The effective (measured) NRCS σ_{eff} at wind speed U , nominal incidence angle θ_0 , and azimuth ϕ_0 is a convolution of the true sea surface NRCS σ_o and the radar antenna pattern Γ_{eff}

$$\begin{aligned} \sigma_{\text{eff}}(\theta_0, \phi_0, U) &= \frac{\int \Gamma_{\text{eff}}(x, y) \sigma_o(x, y, U) dx dy}{\int \Gamma_{\text{eff}}(x, y) dx dy} \\ &= \frac{\int \Gamma_{\text{eff}}(\theta, \phi) \sigma_o(\theta, \phi, U) J(\theta, \phi) d\theta d\phi}{\int \Gamma_{\text{eff}}(\theta, \phi) J(\theta, \phi) d\theta d\phi} \quad (4) \end{aligned}$$

where $J(\theta, \phi)$ is the Jacobian of $\{x, y\}$ - to $\{\theta, \phi\}$ -coordinate transformation and $dx dy = J(\theta, \phi) d\theta d\phi$ (see Appendix C).

To obtain the true NRCS $\sigma_o(\theta, \phi, U)$ from the measured NRCS $\sigma_{\text{eff}}(\theta_0, \phi_0, U)$, integral equation (4) is solved numerically by minimizing the norm of residuals between the measured σ_{eff} and a fitting model for σ_o . Following [13] and [27], the fitting model is represented as a truncated Fourier series

$$\sigma_o = A_0(\theta, U) + A_1(\theta, U) \cos \phi + A_2(\theta, U) \cos 2\phi \quad (5)$$

where coefficients A_j are functions of U and θ .

Note that Ka-band Bragg waves are strongly affected by viscous dissipation, which in turn depends on sea surface temperature (SST) [28]. However, we do not consider SST dependence of the NRCS because our data are collected in a relatively narrow SST range between 18 °C and 22 °C.

The observed σ_{eff} varies in a wide range, from 10 to 15 dB at near-nadir angles to -40 dB (after noise removal) at high incidence angles. For such a large dynamical range, the minimization is more effective for σ_o represented in logarithmic units. Therefore, instead of (5), the true NRCS is fitted by the following model:

$$\log \sigma_o = A_0(\theta, U) + A_1(\theta, U) \cos \phi + A_2(\theta, U) \cos 2\phi \quad (6)$$

with coefficients A_j represented as polynomials of θ and $\log U$

$$A_j = \sum_{m=0}^4 \sum_{k=0}^1 C_{mjk} \theta^m (\log U)^k. \quad (7)$$

Since the number of measurements is of the order of 1000, the system of linear equations (6) is overdetermined and unknown coefficients C_{mnk} (30 per each polarization; see Appendix D) are obtained by minimizing the least square error. The true NRCS $\sigma_o(\theta, \phi, U)$ satisfies nonlinear integral equation (4), which is solved iteratively using the Nelder–Mead simplex (direct search) method [29] starting from a first guess based on fitting model (6) for the measured NRCS (shown by solid lines in Fig. 5). Logarithmic scale (6) is used only for data fitting, while the resulting empirical fit is transformed back into linear units.

B. Accuracy Testing

The accuracy of the fitting method is checked by applying the angular antenna pattern to the solution of (6) and comparing the results with the measured NRCS (Fig. 6). The model root-mean-square errors are found to be 1.47 and 1.50 dB for

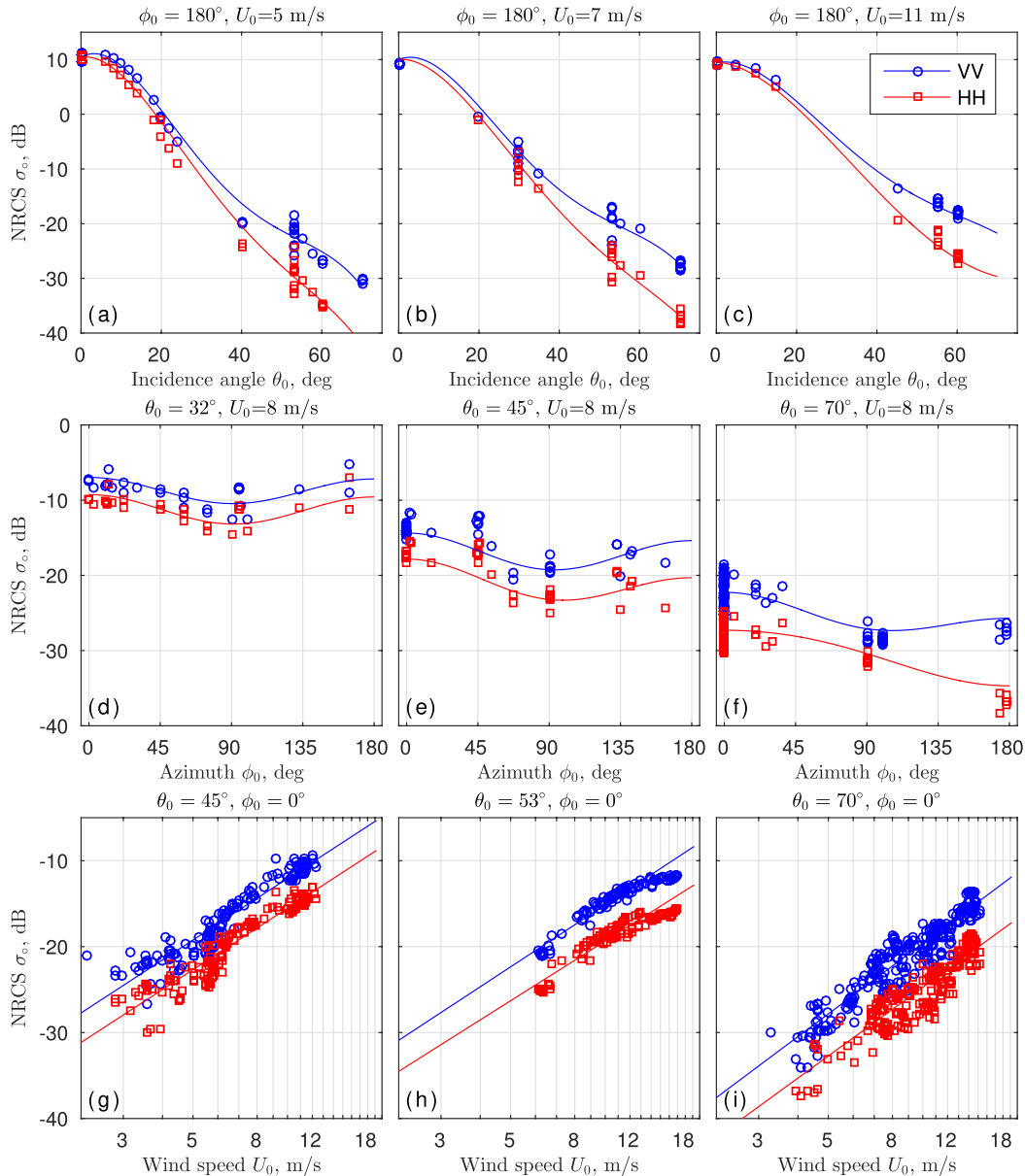


Fig. 5. Measured NRCS versus (a)–(c) incidence angle, (d)–(f) azimuth, and (g)–(i) wind speed. The radar look geometry and wind speed are given in the legends. Solid lines: best data fit in form of (6). Blue curve: VV polarization. Red curve: HH polarization.

VV and HH polarizations, respectively, with 0.98 correlation coefficient.

The limits of applicability of our empirical model [Ka-band dual PP empirical model (KaDPMoD)] are defined by the range of observed conditions and technical limitations of the radar. The minimum detectable wind speed at moderate incidence angles is about 3 m/s and is determined by the radar noise. The maximum observed wind speed is 18 m/s. Since the fit is less confident at low incidence angles (due to poor statistics), we suggest using KaDPMoD at $25^\circ < \theta < 65^\circ$, where the upper incidence angle limit is also imposed by the radar noise.

C. “True” NRCS

Because the KaDPMoD does not depend on the technical characteristics of our particular radar, it can be compared with

independent Ka-band data [15], [20], [21] and the Ku-band PP backscatter NSCAT-4 model [30] (Figs. 7–9).

In general, KaDPMoD is systematically higher by 5–10 dB than MOSN’86 (see also the discussions in [17] and [18]). However, the KaDPMoD agrees well with Plant *et al.*’s. [20] PP data collected in the near-upwind direction at $\theta = 45^\circ$ [Fig. 9(b)]. Giovanangeli *et al.*’s. [21] laboratory VV measurements are available at $\theta = 30^\circ$ for all azimuths. The KaDPMoD agrees well with [21] in the upwind direction [Fig. 9(a)], but is 2–4 dB lower in the downwind and crosswind directions (not shown).

The comparison of KaDPMoD with the Ku-band NSCAT-4 model reveals quite reasonable correspondence at high incidence angles, $\theta > 45^\circ$. However, the KaDPMoD significantly exceeds NSCAT-4 at lower incidence angles (Fig. 7). In particular, the difference reaches 5 dB at $\theta = 30^\circ$ and $U = 5$

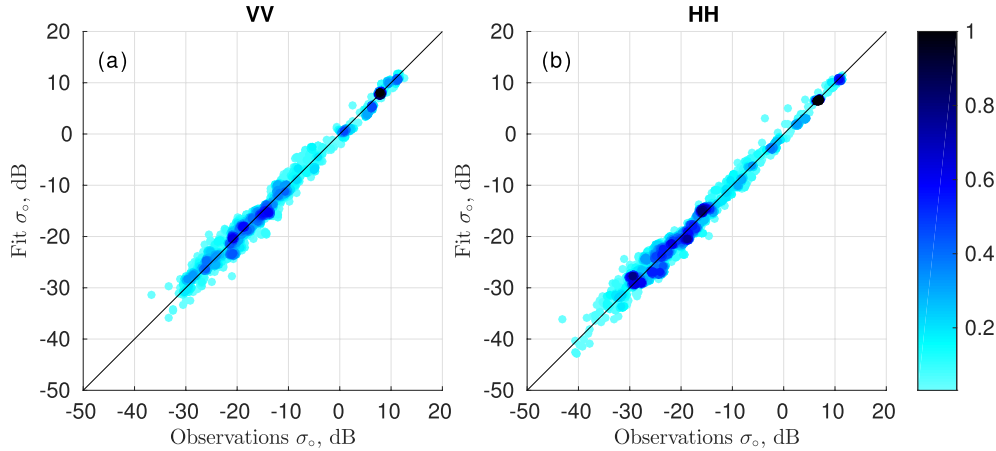


Fig. 6. Scatter diagram of the measured NRCS and true NRCS weighted with the radar antenna pattern (4) for (a) VV and (b) HH polarizations. The color indicates the density of data points.

m/s in the downwind direction [Fig. 7(c)]. Both KaDPMOD and NSCAT-4 models have a similar azimuth dependence at rather strong winds, $U \geq 10$ m/s (Fig. 8). However, at weaker winds, $U = 5$ m/s, the azimuth dependence of the Ka-band NRCS becomes stronger than that of the Ku-band NRCS.

At low incidence angles, $\theta < 30^\circ$, the upwind–downwind difference is near zero or negative (in decibels) [Fig. 10(a)–(c)]. At larger incidence angles, this difference grows up to more expected positive values and even becomes stronger than that in the Ku-band for both polarizations.

In general, the Ka-band upwind–crosswind difference is similar to that in the Ku-band. It has maximum values at moderate incidence angles, $40^\circ < \theta < 50^\circ$. However, at large incidence angles, $\theta \sim 60^\circ$, the crosswind Ka-band HH NRCS becomes higher than that in the downwind direction and causes a unimodal azimuth distribution (Figs. 8 and 10). Except at low winds, both KaDPMOD and MOSN’86 predict consistent values of the upwind–downwind and upwind–crosswind NRCS difference.

IV. DUAL COPOLARIZED FEATURES

The KaDPMOD is further analyzed in terms of the NRCS decomposition into the polarized Bragg component [described by the two-scale model (TSM)] and nonpolarized (NP) (scalar) components. Following [31], the NRCS (in linear units) is represented as

$$\sigma_o^{\text{pp}} = \sigma_{\text{br}}^{\text{pp}} + \sigma_{\text{np}} \quad (8)$$

where the superscript (pp) stands for polarization. The NP component is associated with quasi-specular reflection from steep breaking waves and regular (nonbreaking) surface. The latter is important at small incidence angles, $\theta < 20^\circ$, but in the Ka-band (in contrast to the C- and Ku-bands), it could contribute to the NRCS at larger θ due to a wider spectral interval of long waves (LWs) tilting the Bragg waves. Given known VV and HH NRCSs, the NP term, σ_{np} , can be estimated from a combination of the TSM polarization ratio (PR) (P_{br})

and observed polarization difference (PD) ($\Delta\sigma$)

$$\sigma_{\text{np}} = \sigma_o^{\text{vv}} - \frac{\Delta\sigma}{1 - P_{\text{br}}^{-1}} \quad (9)$$

$$P_{\text{br}} = \sigma_{\text{br}}^{\text{vv}} / \sigma_{\text{br}}^{\text{hh}} \quad (10)$$

$$\Delta\sigma \equiv \sigma_o^{\text{vv}} - \sigma_o^{\text{hh}} = \sigma_{\text{br}}^{\text{vv}} - \sigma_{\text{br}}^{\text{hh}}. \quad (11)$$

Anticipating that Ka-band scattering is quite complicated and significantly affected by the LW (via tilting, hydrodynamic modulations, and nonlinearity of the surface slopes), we restrict our analysis to moderate incidence angles, $\theta > 30^\circ$. Then the TSM solution can be represented as the first two terms of a Taylor expansion in the LW slope (see [32], [33])

$$\sigma_{\text{br}}^{\text{pp}} = \pi G_{\text{pp}}^2 B(\mathbf{k}_{\text{br}}) \left(1 + g_{\text{pp}} \overline{\zeta_i^2} - \frac{M_t^{\text{pp}}}{B} \overline{\zeta_i \tilde{B}} \right) \quad (12)$$

where $G_{\text{pp}}^2 = G_{0\text{pp}}^2 \sin^{-4} \theta$, $G_{0\text{pp}}$ are the “classical” Bragg scattering coefficients (see [34], [35]), $B(\mathbf{k}_{\text{br}})$ is the folded saturation spectrum at Bragg wavenumber $k_{\text{br}} = 2k_r \sin \theta$, k_r is the radar wavenumber, B is the Bragg spectrum variation due to the LW, $\overline{\zeta_i^2}$ is the LW mean square slope in the incidence plane direction, and the tilt modulation transfer function (MTF) M_t^{pp} is

$$M_t^{\text{pp}} = G_{\text{pp}}^{-2} \frac{\partial G_{\text{pp}}^2}{\partial \theta}.$$

The geometric coefficients g_{pp} in (12) are

$$g_{\text{vv}} = \frac{1}{2G_{\text{vv}}^2} \frac{\partial^2 G_{\text{vv}}^2}{\partial \theta^2} \quad (13)$$

$$g_{\text{hh}} = \frac{1}{2G_{\text{hh}}^2} \frac{\partial^2 G_{\text{hh}}^2}{\partial \theta^2} + \frac{2}{\sin^2 \theta} \frac{|G_{\text{vv}}| \overline{\zeta_c^2}}{|G_{\text{hh}}| \overline{\zeta_i^2}} \quad (14)$$

where $\overline{\zeta_c^2}$ is the LW mean square slope in the direction normal to the radar incidence plane.

Representing the Bragg wave modulations via the hydrodynamic MTF, $\tilde{B}/B = M_h k a$, where a is the wave amplitude, and disregarding the spectral dependence of M_h , the mean contribution to NRCS in (12) arising from the correlation

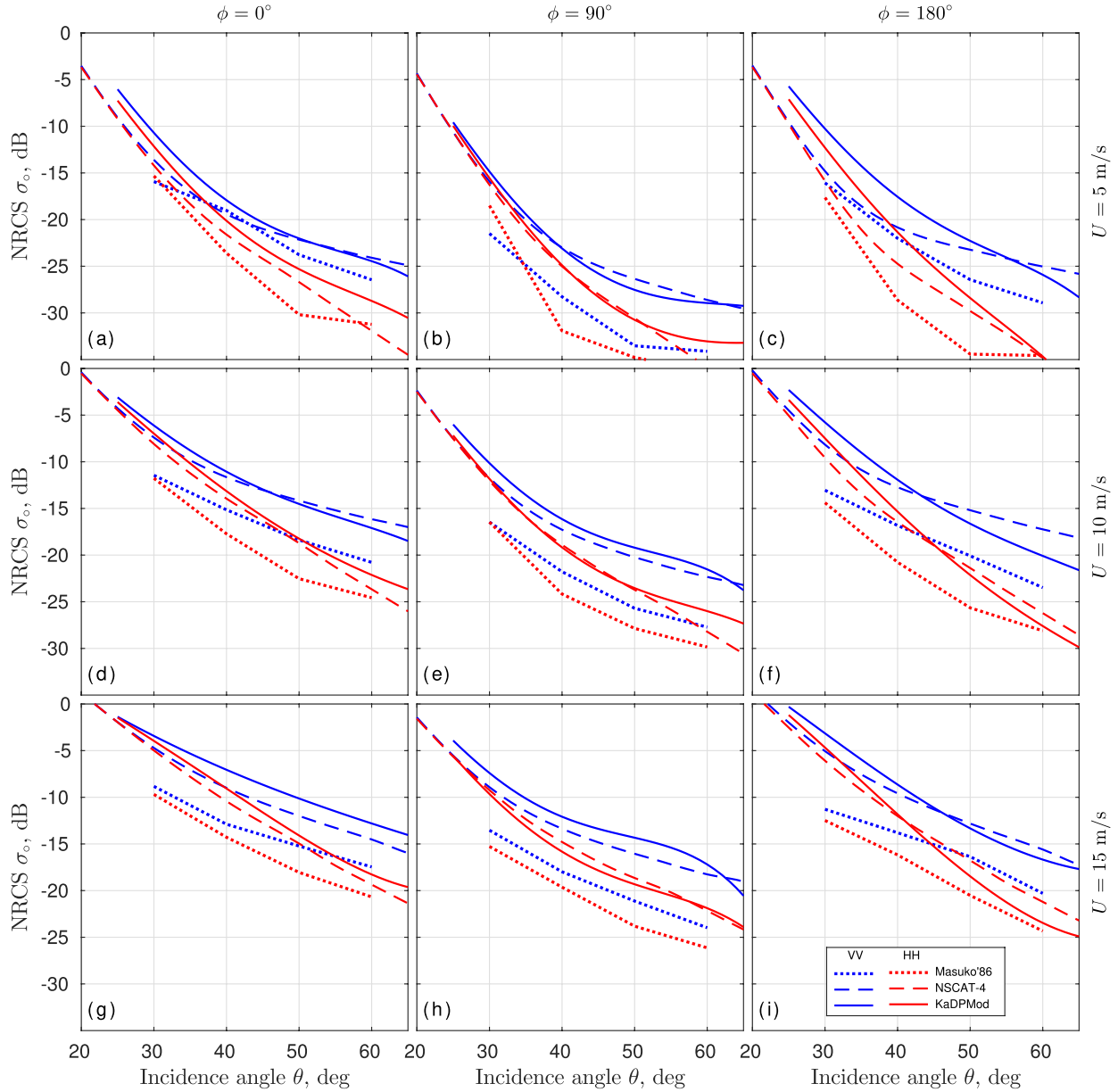


Fig. 7. Dependence of NRCS on incidence angle. Left: upwind direction. Middle: crosswind direction. Right: downwind direction. Top to bottom: wind speeds are 5, 10, and 15 m/s, respectively. Blue curves: VV polarization. red curves: HH polarization. Solid curves: KaDPMoD. Dashed curves: Ku-band NSCAT-4. Dotted curves: MOSN'86.

between the tilt and hydrodynamic modulations can be written as $(M_i^{pp}/B)\zeta_i \bar{B} = -M_i^{pp} M_h^I \zeta_i^2 \cos \phi$, where M_h^I is the imaginary part of the hydrodynamic MTF, whose sign is chosen so that $M_h^I > 0$ if the Bragg waves enhance on the forward (downwind) slope of the LW. Then, (12) can be rewritten as

$$\sigma_{br}^{pp} = \pi G_{pp}^2 B(\mathbf{k}_{br}) (1 + g_{pp} \zeta_i^2 + h_{pp} \zeta_i^2 \cos \phi) \quad (15)$$

$$h_{pp} = M_i^{pp} M_h^I. \quad (16)$$

A. Polarization Ratio

The PR is a direct indicator of the relative contribution of different backscattering mechanisms. Depending on the relative NP contribution, the PR varies from 1 (if NP scattering

dominates) to P_{br} (if NP scattering is negligible)

$$P = \frac{\sigma_{br}^{vv} + \sigma_{np}}{\sigma_{br}^{hh} + \sigma_{np}}. \quad (17)$$

The relative roles of the Bragg and NP components are evaluated from observed PR and corresponding TSM PR. The latter is computed without accounting for the hydrodynamic modulations [see the last term in (15) is omitted]. For the sake of simplicity, the LW mean square slope is estimated from the Phillips saturation spectrum [36], $\zeta^2 = 4.6 \times 10^{-3} \ln(k_d/k_p)/2$, where $k_p = g/U^2$ is the peak wavenumber and $k_d = k_{br}/4$ is the dividing wavenumber. Note that TSM PR does not depend on the Bragg wave spectrum but is a function of θ and weakly depends on wind speed via the LW slope.

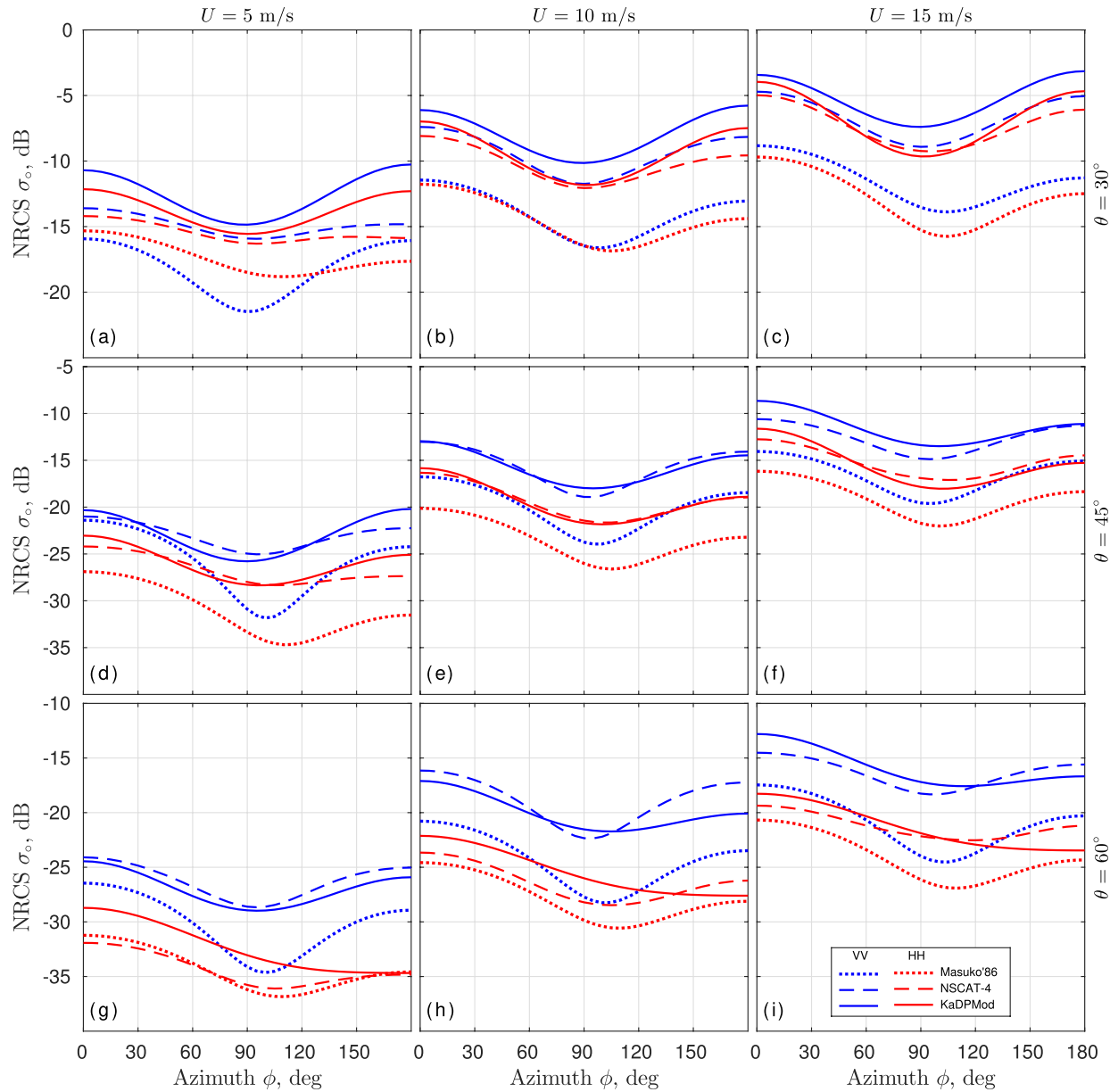


Fig. 8. Azimuth dependence of NRCS at the wind speeds of 5 (left), 10 (middle), and 15 m/s (right). Top to bottom: incidence angles are 30° , 45° , and 60° . The colors and line styles are the same as in Fig. 7.

Both Ka- and Ku-band PRs are lower than TSM PR indicating a non-negligible NP scattering (Fig. 11). The observed PR is closer to the Bragg TSM PR in the downwind direction where the NP scattering by breaking waves is minimal. At $\theta < 55^\circ$, the PR is minimal in the upwind direction suggesting that the impact of the NP component is the strongest in this direction. At $\theta > 55^\circ$, the maximal impact of NP shifts to the crosswind direction where Bragg scattering is weak. In general, the Ka-band PR is qualitatively similar to that in the Ku-band, except for $\theta > 45^\circ$ where the Ka-band PR is lower due to stronger NP scattering by breaking waves.

The upwind and crosswind PRs increase with the wind toward TSM PR [Fig. 11(b)]. This suggests that wind growth rate of capillary Bragg waves is stronger than wind growth rate of wave breaking responsible for NP scattering. Remarkably, this feature distinguishes the Ka-band from the Ku-band

[Fig. 11(b)] and the C-band [37], for which the relative role of the Bragg backscattering weakens as the wind strengthens.

B. Polarization Difference

By definition (11), the PD does not include the NP backscattering, and thus it describes only Bragg scattering characteristics. The Bragg waves and thus PD are strongly wind dependent (Fig. 12). Both Ka- and Ku-band PDs demonstrate strong wind directionality with an apparent minimum in the crosswind direction. The KaDPMoD wind exponents are about 2.5 and 2 in the upwind and downwind directions, respectively. The Ku-band NSCAT-4 wind exponents are about 2 in these two directions. In the crosswind direction, the KaDPMoD wind exponent (~ 3) exceeds its

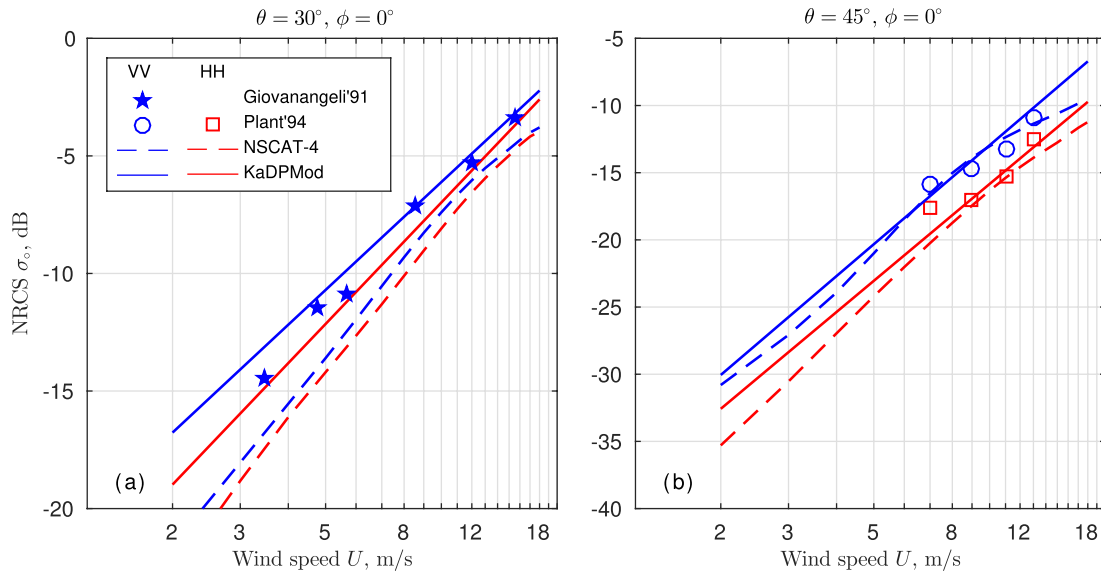


Fig. 9. Wind speed dependence of upwind NRCS at (a) $\theta = 30^\circ$ and (b) $\theta = 45^\circ$. The colors and line styles are the same as in Fig. 7.

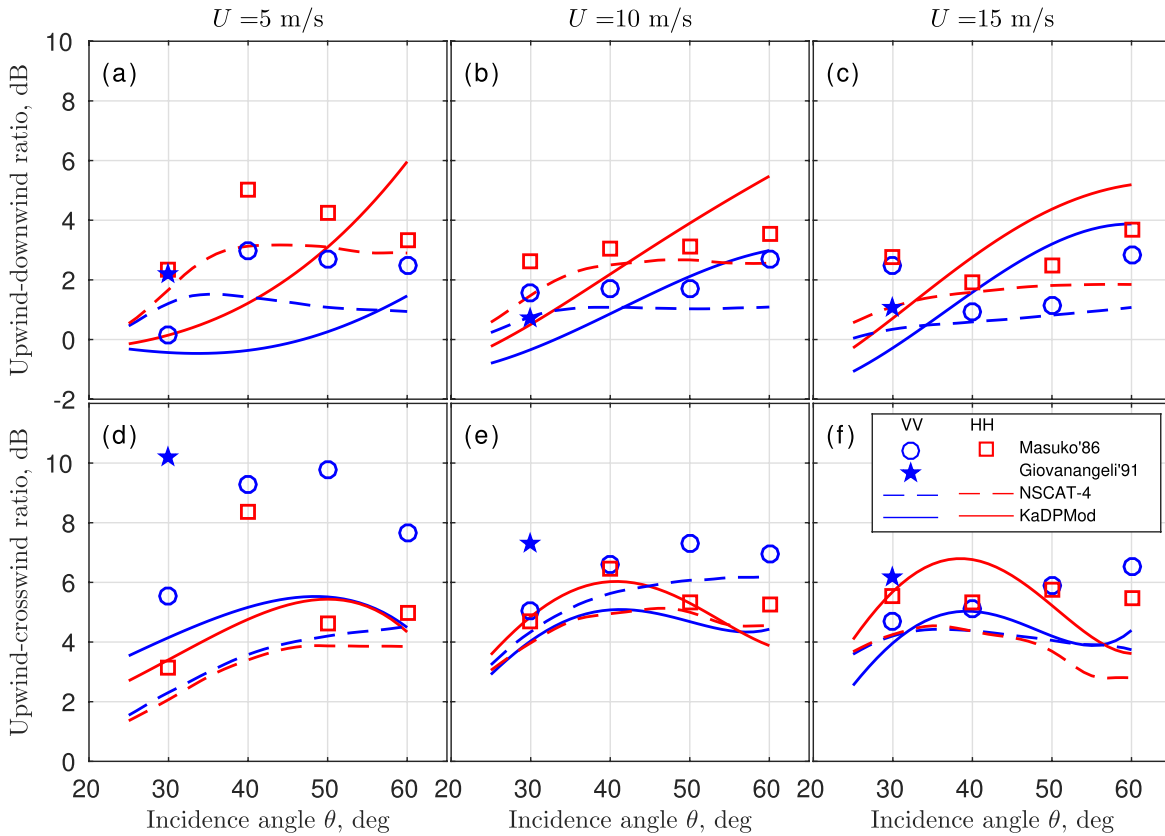


Fig. 10. (a)–(c) Upwind–downwind and (d)–(f) upwind–crosswind NRCS ratios at $U = 5$ -, 10 -, and 15 -m/s versus incidence angles. The colors and linestyles are the same as in Fig. 7.

upwind and downwind values. This is in contrast to the Ku-band, which has a lower crosswind wind exponent < 2 .

The upwind–downwind asymmetry of PD has a more complicated behavior. In the frame of the Bragg TSM, this asymmetry is attributed to the correlation of Bragg wave energy with the tilting LW slopes [see the last term in (15)], which is positive/negative if Bragg roughness enhances on

forward/backward slopes, respectively. The Ka- and Ku-band models suggest that both signs of upwind–downwind asymmetry are possible. In particular, the downwind PD is larger than upwind PD at $\theta < \sim 45^\circ$ for $U = 10$ m/s and *vice versa* at larger incidence angles [Fig. 12(a)]. Interestingly, those Ka- and Ku-band PD asymmetries both change sign at the same $\theta \approx 43^\circ$ for $U = 10$ m/s. At a fixed $\theta = 45^\circ$, the

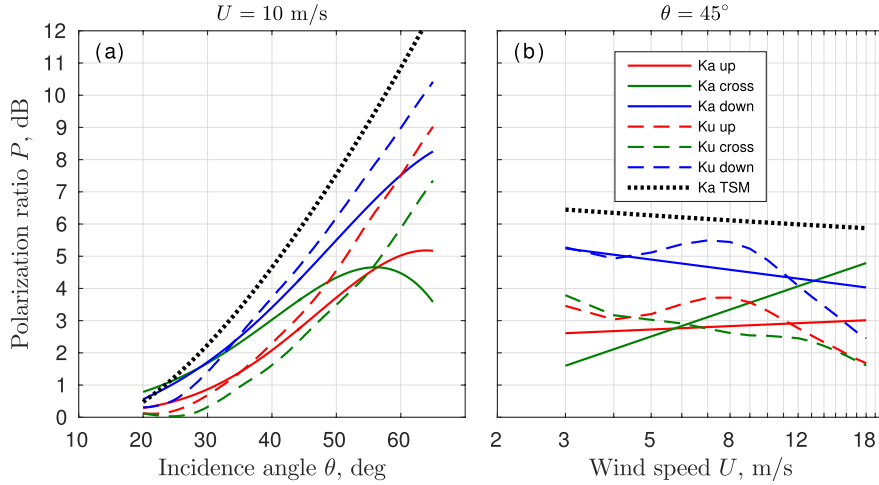


Fig. 11. PR as a function of (a) incidence angle at $U = 10$ m/s and (b) wind speed at $\theta = 45^\circ$ from KaDPMoD (solid lines), Ku-band NSCAT-4 (dashed lines), and Bragg TSM (black dotted lines) for the upwind (red curve), crosswind (blue curve), and downwind (green curve) directions.

Ka-band upwind–downwind PD asymmetry is wind dependent [Fig. 12(b)]. At $U \approx 10$ m/s, the KaDPMoD downwind PD is larger than upwind PD, but this asymmetry changes sign at stronger winds. However, at $\theta = 45^\circ$, the Ku-band upwind and downwind PDs are almost identical.

The presence of Ka-band PD absolute maximum in the upwind direction at high winds and large incidence angles (Fig. 12) is expected due to the effect of enhancement of the parasitic capillary (bound) waves on the forward slopes of the LW. However, the origin of the downwind absolute maximum of PD, which is observed at lower winds and smaller incidence angles in the Ka-band and Ku-band, as well as in the C-band [24], is not clear. Here, we may only speculate that it is probably caused by the small scale roughness covering the backward slopes of breaking waves, which dominates the upwind–downwind asymmetry at low incidence angles, $\theta < 45^\circ$. At the larger incidence angles, the Bragg roughness (including parasitic capillaries) covering the forward breaking wave slope, which is steeper than backward, dominates the asymmetry.

C. Bragg Wave Spectrum Retrieval

Following the Bragg TSM paradigm, the Bragg wave spectrum $B(\mathbf{k}_{br})$ can be estimated from the observed PD using (15) rewritten as:

$$\Delta\sigma = \pi B(\mathbf{k}_{br}) [\Delta(s_{pp}) + \Delta(G_{pp}^2 h_{pp}) \overline{\zeta^2} \cos\phi] \quad (18)$$

where $s_{pp} = G_{pp}^2 (1 + g_{pp} \overline{\zeta^2})$ and $\Delta(f_{pp}) = f^{vv} - f^{hh}$. Representing the Bragg wave saturation spectrum in the same way as in [38]

$$B(\mathbf{k}_{br}) = \frac{1}{2\pi} B_o(k_{br})(1 + \delta \cos 2\phi) \quad (19)$$

where $B_o(k_{br}) = \int_0^{2\pi} B(k_{br}, \phi) d\phi$ is the omnidirectional saturation spectrum and δ is the angular width parameter,

using (5) and (19), we have

$$\Delta\sigma \approx A_0^{PD} + A_1^{PD} \cos\phi + A_2^{PD} \cos 2\phi \quad (20)$$

$$A_0^{PD} = B_o(k_{br}) \Delta(s_{pp}) / 2 \quad (21)$$

$$A_1^{PD} = B_o(k_{br}) \Delta(G_{pp}^2 h_{pp}) \overline{\zeta^2} / 2 \quad (22)$$

$$A_2^{PD} = B_o(k_{br}) \Delta(s_{pp}) \delta / 2. \quad (23)$$

The coefficients A_j^{PD} in (20) are estimated from observations [see Appendix D, with $\Delta\sigma$ instead of σ_o in (40)–(42)]. The omnidirectional spectrum and the angular width parameter are calculated using (16) and (21)–(23) and observation-based coefficients A_j^{PD}

$$B_o(k_{br}) = 2A_0^{PD} / \Delta(s_{pp}) \quad (24)$$

$$\delta = A_2^{PD} / A_0^{PD}. \quad (25)$$

The estimates of B_o and δ retrieved from the Ka-band PD as well as from the Ku-band NSCAT-4 and C-band C-SARMOD [24] are compared with optically based field measurements [38], [39] (Fig. 13).

Radar-derived wave spectra demonstrate stronger wind dependence and higher levels in the capillary range. The latter suggests that the parasitic capillary (bound) mechanism plays a crucial role in the establishing of the spectral level of capillary waves. Although radar and optical spectra are very roughly similar in spectral level, the radar spectra are about two times higher. The possible origin of such a difference is in the way that the two kinds of spectra are derived. Optical spectra are normally derived from wave breaking-free images, while radar spectra account for the entire sea surface backscattering including rough patterns of breaking waves. Therefore, the difference between the radar and the optical spectra can be treated as an impact of surface roughness covering wave breaking zones. Optical spectra from [38] and our radar spectra clearly indicate the presence of a peak in the saturation spectra in the capillary range around $k = 1000$ rad/m originating from the generation of parasitic capillaries. In that respect, our measurements deviate from recent optical polarimetric

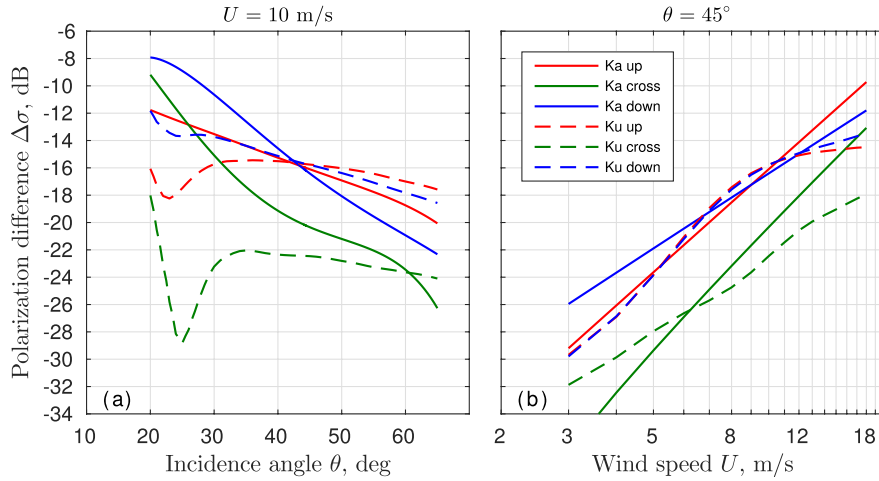
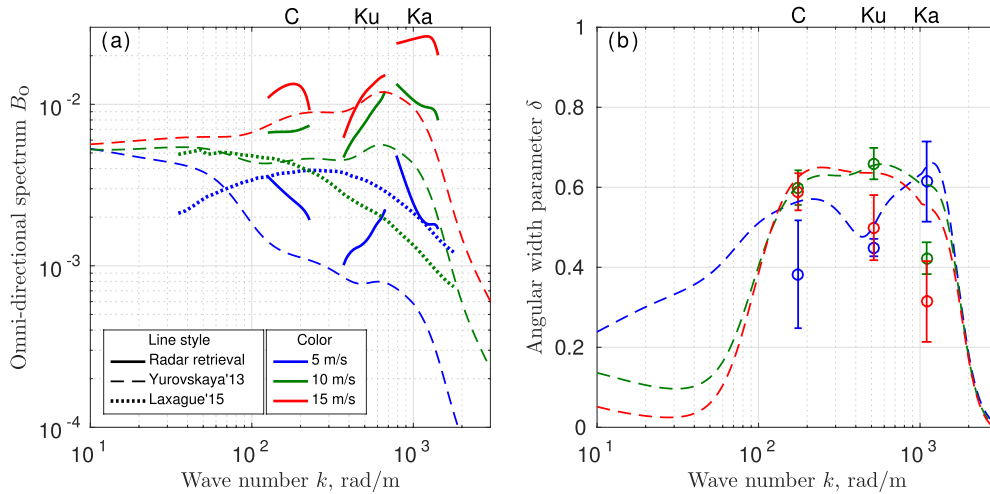


Fig. 12. Same as Fig. 11, but for PD without TSM prediction.

Fig. 13. (a) Omnidirectional saturation spectra B_0 and (b) angular width parameter δ estimated from radar PD for C- (C-SARMOD), Ku- (NSCAT-4), and Ka-band (KaDPMoD) in comparison with optical measurements [38], [39].

measurements [39], which show a decrease in spectral level at wavenumbers above $k = 360$ rad/m.

The angular width of radar spectra, $\delta \approx 0.5$, indicates that the Bragg crosswind wave energy is about three times lower than the wave energy in the downwind direction, which qualitatively agrees with optical measurements [38] [Fig. 13(b)]. The angular distribution of radar spectra is weakly wind dependent. It is quite narrow in the capillary and capillary-gravity range and becomes much wider in the short gravity wave range.

D. Nonpolarized Contribution

The Ka- and Ku-band NP components of NRCS, σ_{np} , estimated from the corresponding model functions using (9) show general consistency in magnitude as well as their dependency on wind speed and incidence angle (Fig. 14). Nevertheless, some important differences in their azimuth

variations are present. While the azimuth distribution of Ku-band NP backscattering is unimodal (with a maximum in the upwind direction), the Ka-band azimuth distribution is bimodal at $\theta < 50^\circ$ (with a minimum in the crosswind direction) and becomes unimodal only at larger incidence angles [Fig. 14(a)]. Such a unimodal azimuth distribution of σ_{np} can occur if the NP is dominated by a radar return from the forward slope of breaking waves. This is plausible at large incidence angles when the local incidence angle on the backward wave slope is rather large and the corresponding backscattering is weak. At moderate incidence angles, a bimodal azimuth distribution of NP backscattering is feasible if the NP from “enhanced” roughness on the backward slope of breaking waves becomes comparable to NP backscattering from the forward slopes.

The wind exponent of the Ka-band NP component is close to 2 [Fig. 14(b)]. This wind exponent is in contrast to the cubic wind dependence of whitecap areal coverage usually considered as an indicator of wave breaking [40]. However, the sea surface radar backscattering is sensitive to very different

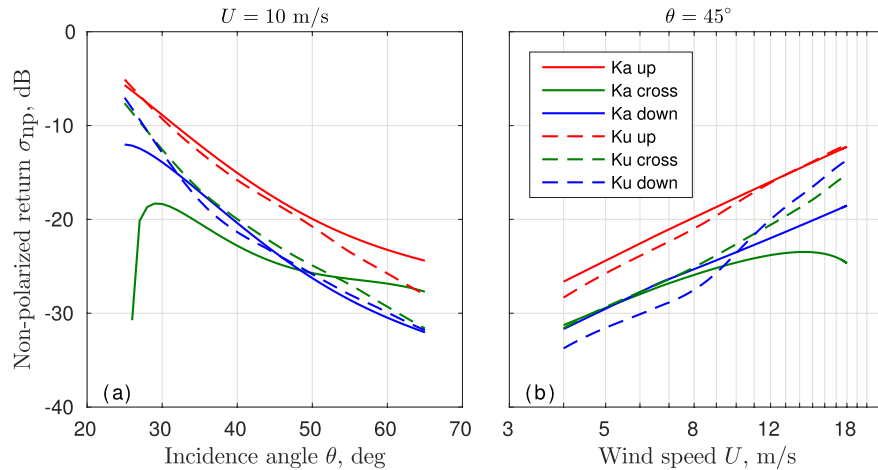


Fig. 14. NP NRCS component versus (a) incidence angle and (b) wind speed for upwind (red curve), crosswind (green curve), and downwind (blue curve) directions from KaDPMoD (solid curve) and Ku-band NSCAT-4 (dashed curve).

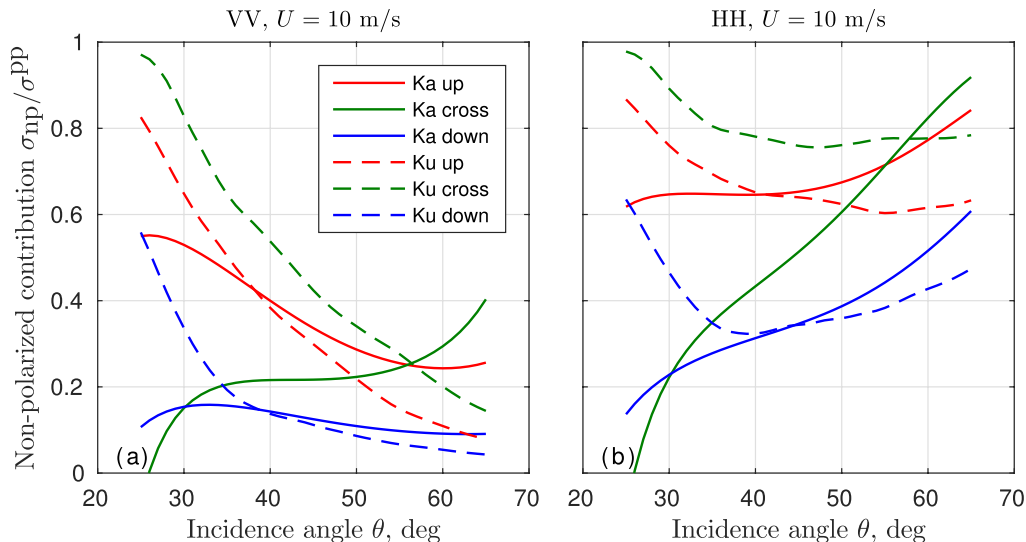


Fig. 15. Partial contribution of NP radar backscattering to total NRCS versus incidence angle for (a) VV and (b) HH polarizations. The colors and line styles are the same as in Fig. 14.

parameters of wave breaking, which are not directly associated with the whitecap areal coverage. One may speculate that NP backscattering is produced by quasi-specular reflections from steep patterns covering breaking wave crests with wavelengths of the order of decimeter and longer scales. These waves belong to the equilibrium range where the wave breaking parameters are proportional to U^2 (see [33] and [41] for more discussions).

The relative contribution of upwind and downwind NP backscattering to the total NRCS has a similar magnitude in the Ka- and Ku-band at $\theta > 40^\circ$ (Fig. 15). At HH polarization, the NP contribution to NRCS becomes dominant in both bands as θ increases [Fig. 15(b)]. At smaller incidence angles, $\theta < 40^\circ$, the relative contribution of the NP is lower in the Ka-band in comparison with the Ku-band. Because the saturation spectrum level is higher at the Ka-band Bragg wavenumber [Fig. 13(a)], comparable magnitudes of NP backscattering provide a relatively smaller

contribution to the Ka-band NRCS in comparison with the Ku-band.

The observed decrease in the relative contribution of the NP to the Ka-band NRCS with increasing wind speed is rather unexpected. However, Figs. 12(b) and 14 suggest that Bragg waves (associated with the PD) grow faster with the wind than the NP term. Therefore, the relative contribution of NP backscattering to the NRCS should decrease with the wind. This behavior is in line with observations in Fig. 16.

V. CONCLUSION

In this paper, we report the Ka-band dual PP (VV and HH) backscattering features of the sea surface derived from measurements collected from the Black Sea Research platform during the seven years of field campaigns between 2009 and 2015. The radar measurements are collected in the incidence angle range: $25^\circ < \theta < 65^\circ$ and the wind

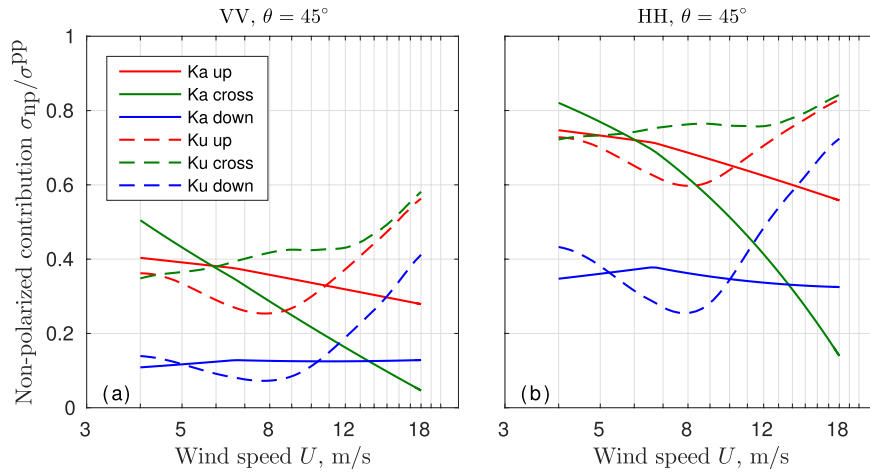


Fig. 16. Partial contribution of NP radar backscattering to total NRCS versus wind speed for (a) VV and (b) HH polarizations. The colors and line styles are the same as in Fig. 14.

speed range: $3 \text{ m/s} < U < 18 \text{ m/s}$, and with the radar-to-wind azimuth varying from upwind to downwind. The radar measurements are corrected for the impact of the antenna angular pattern and are presented in a form of a conventional truncated azimuthal Fourier series with coefficients dependent on the incidence angle and wind speed. This parameterization is referred as a radar backscattering empirical model (KaDPMoD). We anticipate that this empirical model can be used as a first guess for developing Ka-band GMF for the sea surface NRCS.

To the best of our knowledge, KaDPMoD is the first attempt to parametrize the Ka-band sea surface NRCS at moderate incidence angles for both VV and HH polarizations since the MOSN'86 model [15] and its reevaluation [16]. We find that KaDPMoD is 5–10 dB higher than the MOSN'86 data, which is believed to be due (after [17]) to uncertainties in their data calibration. KaDPMoD is consistent with independent Ka-band data collected in the field [20] and also under laboratory conditions [21]. In general, KaDPMoD is consistent with the empirical Ku-band NSCAT-4 model over a wide range of wind speeds and incidence angles. However, there are some remarkable differences between the Ku- and Ka-band models.

To get deeper insight into the physics of Ka-band sea surface backscattering, the dual PP measurements are decomposed into resonant Bragg backscattering and NP backscattering from breaking waves [31]. The relative importance of NP is confirmed by the presence of a significant deviation of the measured PR ($\sigma_o^{vv}/\sigma_o^{hh}$) from the Bragg TSM. Unlike C- and Ku-bands, the Ka-band PR increases strongly with wind toward the TSM PR values. This suggests that the wind-induced growth of Bragg waves is stronger than that of NP backscattering associated with wave breaking.

The PD ($\sigma_o^{vv} - \sigma_o^{hh}$) allows us to eliminate the NP component and provides a direct information about short Bragg waves. Our measurements show that PD and thus Ka-band Bragg waves are strongly wind dependent, with a wind exponent of about 2.5 and 3 in the upwind and crosswind directions, respectively. That is consistent with optical measurements of wave spectra [38], [42]. The PD and thus capillary Bragg

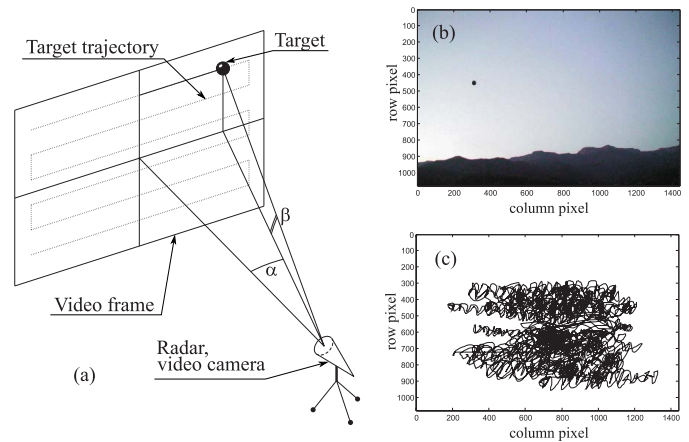


Fig. 17. Radar calibration. (a) Schematic explanation of the method. (b) Target video image on the background of clear skies (mountains at the bottom are tens of kilometers apart). (c) Sample target trajectory.

waves are strongly anisotropic in azimuth with a minimum in the crosswind direction. Upwind-to-crosswind anisotropy is quantitatively consistent with independently measured spectra in the capillary range [38]. However, the upwind-to-downwind asymmetry has a more complex behavior. At $\theta < 45^\circ$ and $U < 10 \text{ m/s}$, the downwind PD exceeds the upwind PD, suggesting that Ka-band Bragg waves are enhanced on the backward slopes of long tilting waves. At larger incidence angles and stronger winds, the PD maximum shifts toward the upwind direction that is anticipated if Bragg waves are mainly generated as parasitic capillaries.

Omnidirectional wave spectra derived from the PD based on KaDPMoD, C-band C-SARMOD [24], and Ku-band NSCAT-4 [30] models provide a quite consistent description of short wind wave spectra and indicate a notable peak in the saturation spectrum level in the capillary–gravity range. This observation is in contrast to [39] suggesting a “slight” roughness contribution from capillary waves and a significant contribution from gravity–capillary waves.

The Ka-band NP NRCS component derived from KaDPMoD is similar to the Ku-band NP derived from the

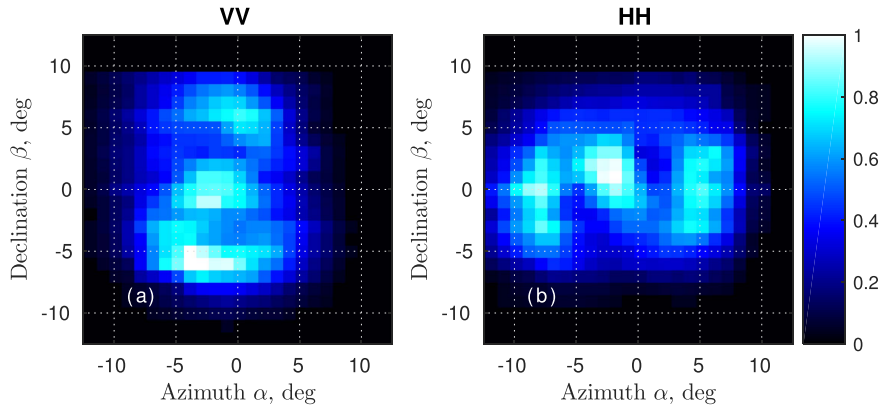


Fig. 18. Normalized two-way radar patterns. (a) Γ^{hh} . (b) Γ^{vv} .

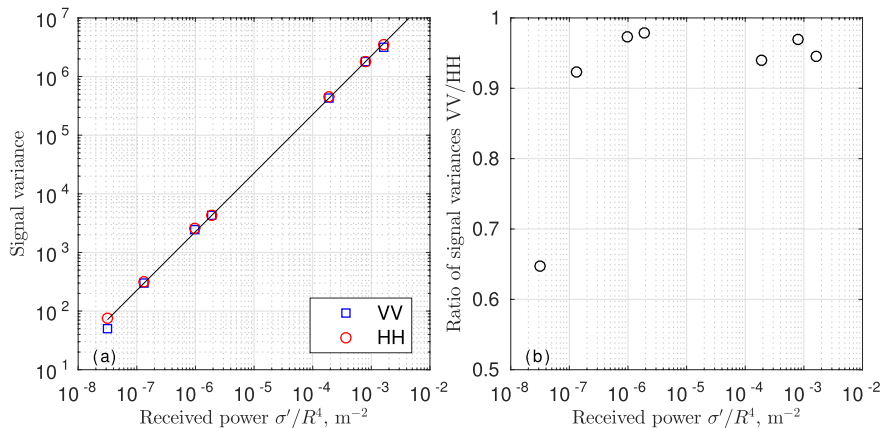


Fig. 19. (a) Dependence of the radar signal variance and (b) ratio of VV and HH variances versus target RCS normalized by the fourth power of distance to the target. The solid line corresponds to the linear fit (calibration curve).

NSCAT-4 empirical model. The relative contribution of the NP component to the total NRCS is significant. In the upwind direction, it is about 60%–80% for HH polarization and about 25%–50% for VV polarization. The NP wind exponent is about 2 in the upwind direction, which is lower than the wind exponent for Ka-band Bragg waves. This explains the decrease in the relative contribution of NP component to the NRCS for both polarizations. Such a wind dependence of the relative NP contribution is opposite to that suggested by the Ku-band NSCAT-4, for which the relative contribution of NP to the total NRCS increases with the wind.

APPENDIX A RADAR CALIBRATION

The radar pattern is crucial for radar calibration and estimation of the effective footprint area. The two-way radar angular antenna pattern is estimated using a metal 100-mm sphere target (installed on thin dielectric lines in front of the radar directed toward the clear sky) and video camera synchronized with the radar (Fig. 17).

Oscillations of the target are synchronously registered by the radar and video camera, thus yielding the radar backscattering as a function of the target's angular coordinates, α and β . The two-way radar pattern Γ is then estimated as the distribution of the received power versus α and β normalized by the peak value (Fig. 18).

The calibration constant C in (1) is estimated from the observations of different targets at known distances and positions within the radar pattern. The relationship between the power received by the radar and the recorded signal power is determined by characteristics of the radar hardware, which may introduce some nonlinearity. For calibration purposes, the received power was varied by changing target type, size, and distance. The relationship between the radar output signal variance and received power is found to be linear in the whole range of signal amplitudes and is used to determine the calibration constant C [Fig. 19(a)]. One can note very close signal levels in both channels [Fig. 19(b)], except for the smallest calibration target with bad signal recognition suggesting that vertical and horizontal channels are well balanced.

APPENDIX B CROSS-POLARIZED CONTAMINATION

The radar hybrid polarization mode results in simultaneous receiving of PP and CP signals in a proportion determined by the radar antenna properties. The complex amplitudes of the vertical V_R and horizontal H_R received signals are

$$\begin{bmatrix} V_R \\ H_R \end{bmatrix} = \begin{bmatrix} R_{vv} & R_{hv} \\ R_{vh} & R_{hh} \end{bmatrix} \begin{bmatrix} S_{vv} & S_{hv} \\ S_{vh} & S_{hh} \end{bmatrix} \begin{bmatrix} T_{vv} & T_{hv} \\ T_{vh} & T_{hh} \end{bmatrix} \begin{bmatrix} V_T \\ H_T \end{bmatrix} \quad (26)$$

where \mathbf{R} and \mathbf{T} are the matrices that describe distortions induced by receive and transmit antennas, respectively, \mathbf{S} is

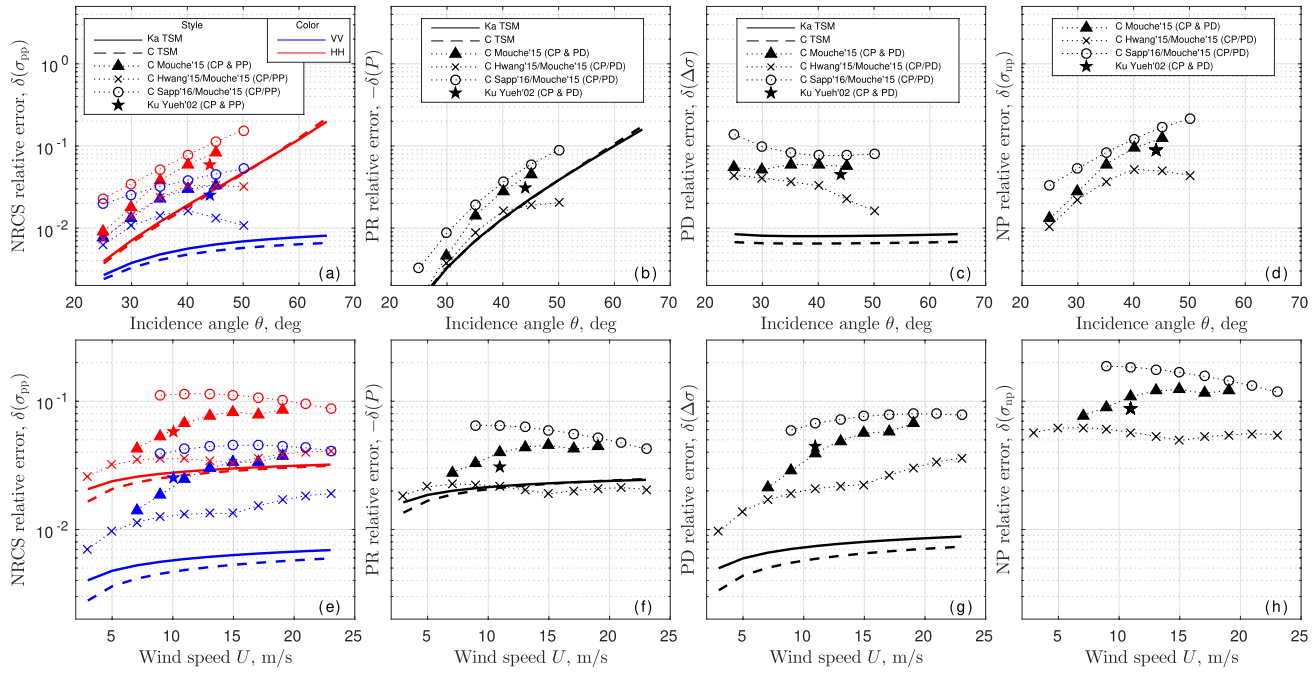


Fig. 20. Relative systematic errors due to the CP component for the (a) and (e) hybrid omnidirectional NRCS (PP + CP), (b) and (f) PR (VV + CP)/(HH + CP), (c) and (g) PD + CP, and (d) and (h) NP term versus (a)–(d) incidence angle θ at $U = 15$ m/s and (e)–(h) wind speed U at $\theta = 45^\circ$ from C- and Ka-band TSM prediction, C-band CP GMFs [24], [25], [45], and C-band PP GMF [24]. The Ku-band measurements at $U = 11$ m/s and $\theta = 44^\circ$ [46] are also shown.

TABLE I
COEFFICIENTS C_{mnk}

Index			C_{mnk}	
m	n	k	VV	HH
0	0	0	$+3.206118 \cdot 10^{+0}$	$+3.287958 \cdot 10^{+0}$
1	0	0	$+1.951546 \cdot 10^{+0}$	$+2.958732 \cdot 10^{-2}$
2	0	0	$-7.208258 \cdot 10^{+1}$	$-6.570137 \cdot 10^{+1}$
3	0	0	$+8.578391 \cdot 10^{+1}$	$+7.779126 \cdot 10^{+1}$
4	0	0	$-2.884517 \cdot 10^{+1}$	$-2.641669 \cdot 10^{+1}$
0	1	0	$-3.791021 \cdot 10^{-2}$	$-6.110719 \cdot 10^{-2}$
1	1	0	$+4.193799 \cdot 10^{+0}$	$+3.088378 \cdot 10^{+0}$
2	1	0	$-1.337898 \cdot 10^{+1}$	$-1.109291 \cdot 10^{+1}$
3	1	0	$+1.119162 \cdot 10^{+1}$	$+1.105847 \cdot 10^{+1}$
4	1	0	$-2.305322 \cdot 10^{+0}$	$-2.403804 \cdot 10^{+0}$
0	2	0	$+1.123723 \cdot 10^{-2}$	$+3.093813 \cdot 10^{-2}$
1	2	0	$+7.798137 \cdot 10^{+0}$	$+6.490559 \cdot 10^{+0}$
2	2	0	$-3.132253 \cdot 10^{+1}$	$-3.154284 \cdot 10^{+1}$
3	2	0	$+4.686008 \cdot 10^{+1}$	$+4.898348 \cdot 10^{+1}$
4	2	0	$-2.244278 \cdot 10^{+1}$	$-2.351261 \cdot 10^{+1}$
0	0	1	$-2.007813 \cdot 10^{-1}$	$-1.435727 \cdot 10^{-1}$
1	0	1	$-1.556322 \cdot 10^{+0}$	$-1.614046 \cdot 10^{+0}$
2	0	1	$+1.779589 \cdot 10^{+1}$	$+1.771247 \cdot 10^{+1}$
3	0	1	$-1.905703 \cdot 10^{+1}$	$-2.040338 \cdot 10^{+1}$
4	0	1	$+5.425915 \cdot 10^{+0}$	$+6.773906 \cdot 10^{+0}$
0	1	1	$+2.754555 \cdot 10^{-2}$	$+2.209574 \cdot 10^{-2}$
1	1	1	$-2.375674 \cdot 10^{+0}$	$-1.987757 \cdot 10^{+0}$
2	1	1	$+7.034096 \cdot 10^{+0}$	$+6.865252 \cdot 10^{+0}$
3	1	1	$-5.337939 \cdot 10^{+0}$	$-6.369661 \cdot 10^{+0}$
4	1	1	$+9.388563 \cdot 10^{-1}$	$+1.467463 \cdot 10^{+0}$
0	2	1	$-4.769737 \cdot 10^{-3}$	$-4.955172 \cdot 10^{-3}$
1	2	1	$-4.252548 \cdot 10^{+0}$	$-3.603769 \cdot 10^{+0}$
2	2	1	$+1.943467 \cdot 10^{+1}$	$+1.922202 \cdot 10^{+1}$
3	2	1	$-2.873040 \cdot 10^{+1}$	$-2.904522 \cdot 10^{+1}$
4	2	1	$+1.330676 \cdot 10^{+1}$	$+1.332051 \cdot 10^{+1}$

the scattering matrix of the target, and V_T and H_T are the intended transmit polarization components, which are equal for our slant polarization mode, $V_T = H_T = 1$.

Assuming a reasonable polarization isolation (about -20 dB for a typical horn antenna), $T_{vh} = T_{hv} = R_{vh} = R_{hv} = 0$, and backscattering reciprocal property, $S_{vh} = S_{hv}$, (26) simplifies to

$$\begin{bmatrix} V_R \\ H_R \end{bmatrix} = \begin{bmatrix} S_{vv}T_{vv}R_{vv} + S_{vh}T_{hh}R_{vv} \\ S_{hh}T_{hh}R_{hh} + S_{vh}T_{vv}R_{hh} \end{bmatrix}. \quad (27)$$

From the calibration by nondepolarizing targets (isotropic spheres and trihedral corner reflectors) with the known scattering coefficients $S' = S'_{vv} = S'_{hh} = \sqrt{\sigma'}$ and $S'_{vh} = S'_{hv} = 0$, some of the polarization distortion parameters can be found

$$\begin{bmatrix} T_{vv}R_{vv} \\ T_{hh}R_{hh} \end{bmatrix} = \begin{bmatrix} V'_R/S' \\ H'_R/S' \end{bmatrix}. \quad (28)$$

The calibration constant for each polarization C_{pp} (1)–(3) can also be determined, $C_{pp} = T_{pp}^2 R_{pp}^2 \cdot (R'^4 / \Gamma')$.

The intended calibrated measurements are

$$\begin{bmatrix} \tilde{S}_{vv} \\ \tilde{S}_{hh} \end{bmatrix} = \begin{bmatrix} V_R/T_{vv}R_{vv} \\ H_R/T_{hh}R_{hh} \end{bmatrix}. \quad (29)$$

For a target with PP return only, the measured scattering coefficients are equal to the PP coefficients, $\tilde{S}_{pp} = S_{pp}$. However, for a target producing the CP, (27) and (29) suggest that the CP signal mixes into the PP signal with coefficients depending on the antenna distortion parameter ratio

$$\begin{bmatrix} \tilde{S}_{vv} \\ \tilde{S}_{hh} \end{bmatrix} = \begin{bmatrix} S_{vv} + S_{vh}T_{hh}/T_{vv} \\ S_{hh} + S_{vh}T_{vv}/T_{hh} \end{bmatrix}. \quad (30)$$

Assuming that CP and PP are not correlated, $\text{Re}(S_{pp}S_{vh}^*) = 0$ (see [43], [44]), the measured scattering

TABLE II
COEFFICIENTS $A_j(\theta, U)$ FOR VV POLARIZATION

$\theta, ^\circ$	Wind speed $U, \text{ m/s}$							
	3	5	7	9	11	13	15	17
	A_0							
25	$+1.05 \cdot 10^{-1}$	$+1.84 \cdot 10^{-1}$	$+2.67 \cdot 10^{-1}$	$+3.52 \cdot 10^{-1}$	$+4.39 \cdot 10^{-1}$	$+5.28 \cdot 10^{-1}$	$+6.18 \cdot 10^{-1}$	$+7.10 \cdot 10^{-1}$
30	$+2.81 \cdot 10^{-2}$	$+6.12 \cdot 10^{-2}$	$+1.02 \cdot 10^{-1}$	$+1.50 \cdot 10^{-1}$	$+2.03 \cdot 10^{-1}$	$+2.62 \cdot 10^{-1}$	$+3.26 \cdot 10^{-1}$	$+3.94 \cdot 10^{-1}$
35	$+9.07 \cdot 10^{-3}$	$+2.36 \cdot 10^{-2}$	$+4.43 \cdot 10^{-2}$	$+7.09 \cdot 10^{-2}$	$+1.03 \cdot 10^{-1}$	$+1.42 \cdot 10^{-1}$	$+1.86 \cdot 10^{-1}$	$+2.35 \cdot 10^{-1}$
40	$+3.70 \cdot 10^{-3}$	$+1.09 \cdot 10^{-2}$	$+2.22 \cdot 10^{-2}$	$+3.81 \cdot 10^{-2}$	$+5.86 \cdot 10^{-2}$	$+8.40 \cdot 10^{-2}$	$+1.14 \cdot 10^{-1}$	$+1.50 \cdot 10^{-1}$
45	$+1.92 \cdot 10^{-3}$	$+6.03 \cdot 10^{-3}$	$+1.30 \cdot 10^{-2}$	$+2.32 \cdot 10^{-2}$	$+3.69 \cdot 10^{-2}$	$+5.46 \cdot 10^{-2}$	$+7.64 \cdot 10^{-2}$	$+1.03 \cdot 10^{-1}$
50	$+1.22 \cdot 10^{-3}$	$+3.93 \cdot 10^{-3}$	$+8.65 \cdot 10^{-3}$	$+1.57 \cdot 10^{-2}$	$+2.55 \cdot 10^{-2}$	$+3.83 \cdot 10^{-2}$	$+5.43 \cdot 10^{-2}$	$+7.39 \cdot 10^{-2}$
55	$+8.88 \cdot 10^{-4}$	$+2.87 \cdot 10^{-3}$	$+6.31 \cdot 10^{-3}$	$+1.15 \cdot 10^{-2}$	$+1.86 \cdot 10^{-2}$	$+2.80 \cdot 10^{-2}$	$+3.97 \cdot 10^{-2}$	$+5.39 \cdot 10^{-2}$
60	$+6.77 \cdot 10^{-4}$	$+2.18 \cdot 10^{-3}$	$+4.73 \cdot 10^{-3}$	$+8.48 \cdot 10^{-3}$	$+1.35 \cdot 10^{-2}$	$+2.00 \cdot 10^{-2}$	$+2.80 \cdot 10^{-2}$	$+3.76 \cdot 10^{-2}$
65	$+5.21 \cdot 10^{-4}$	$+1.58 \cdot 10^{-3}$	$+3.32 \cdot 10^{-3}$	$+5.81 \cdot 10^{-3}$	$+9.14 \cdot 10^{-3}$	$+1.34 \cdot 10^{-2}$	$+1.85 \cdot 10^{-2}$	$+2.47 \cdot 10^{-2}$
	A_1							
25	$+5.86 \cdot 10^{-4}$	$-9.45 \cdot 10^{-3}$	$-2.33 \cdot 10^{-2}$	$-4.00 \cdot 10^{-2}$	$-5.90 \cdot 10^{-2}$	$-7.98 \cdot 10^{-2}$	$-1.02 \cdot 10^{-1}$	$-1.26 \cdot 10^{-1}$
30	$-2.43 \cdot 10^{-3}$	$-4.50 \cdot 10^{-3}$	$-6.66 \cdot 10^{-3}$	$-8.83 \cdot 10^{-3}$	$-1.10 \cdot 10^{-2}$	$-1.31 \cdot 10^{-2}$	$-1.52 \cdot 10^{-2}$	$-1.71 \cdot 10^{-2}$
35	$-1.55 \cdot 10^{-3}$	$-1.89 \cdot 10^{-3}$	$-9.60 \cdot 10^{-4}$	$+1.54 \cdot 10^{-3}$	$+5.78 \cdot 10^{-3}$	$+1.19 \cdot 10^{-2}$	$+2.00 \cdot 10^{-2}$	$+3.03 \cdot 10^{-2}$
40	$-8.55 \cdot 10^{-4}$	$-7.06 \cdot 10^{-4}$	$+9.03 \cdot 10^{-4}$	$+4.45 \cdot 10^{-3}$	$+1.03 \cdot 10^{-2}$	$+1.88 \cdot 10^{-2}$	$+3.01 \cdot 10^{-2}$	$+4.46 \cdot 10^{-2}$
45	$-4.78 \cdot 10^{-4}$	$-1.37 \cdot 10^{-4}$	$+1.51 \cdot 10^{-3}$	$+4.93 \cdot 10^{-3}$	$+1.05 \cdot 10^{-2}$	$+1.86 \cdot 10^{-2}$	$+2.96 \cdot 10^{-2}$	$+4.36 \cdot 10^{-2}$
50	$-2.56 \cdot 10^{-4}$	$+1.82 \cdot 10^{-4}$	$+1.70 \cdot 10^{-3}$	$+4.68 \cdot 10^{-3}$	$+9.42 \cdot 10^{-3}$	$+1.62 \cdot 10^{-2}$	$+2.53 \cdot 10^{-2}$	$+3.69 \cdot 10^{-2}$
55	$-9.15 \cdot 10^{-5}$	$+3.93 \cdot 10^{-4}$	$+1.73 \cdot 10^{-3}$	$+4.19 \cdot 10^{-3}$	$+7.97 \cdot 10^{-3}$	$+1.33 \cdot 10^{-2}$	$+2.03 \cdot 10^{-2}$	$+2.91 \cdot 10^{-2}$
60	$+3.92 \cdot 10^{-5}$	$+5.13 \cdot 10^{-4}$	$+1.62 \cdot 10^{-3}$	$+3.54 \cdot 10^{-3}$	$+6.40 \cdot 10^{-3}$	$+1.03 \cdot 10^{-2}$	$+1.55 \cdot 10^{-2}$	$+2.19 \cdot 10^{-2}$
65	$+1.05 \cdot 10^{-4}$	$+4.98 \cdot 10^{-4}$	$+1.33 \cdot 10^{-3}$	$+2.71 \cdot 10^{-3}$	$+4.75 \cdot 10^{-3}$	$+7.56 \cdot 10^{-3}$	$+1.12 \cdot 10^{-2}$	$+1.58 \cdot 10^{-2}$
	A_2							
25	$+4.52 \cdot 10^{-2}$	$+7.41 \cdot 10^{-2}$	$+1.03 \cdot 10^{-1}$	$+1.31 \cdot 10^{-1}$	$+1.58 \cdot 10^{-1}$	$+1.86 \cdot 10^{-1}$	$+2.13 \cdot 10^{-1}$	$+2.40 \cdot 10^{-1}$
30	$+1.34 \cdot 10^{-2}$	$+2.84 \cdot 10^{-2}$	$+4.67 \cdot 10^{-2}$	$+6.77 \cdot 10^{-2}$	$+9.09 \cdot 10^{-2}$	$+1.16 \cdot 10^{-1}$	$+1.44 \cdot 10^{-1}$	$+1.73 \cdot 10^{-1}$
35	$+4.84 \cdot 10^{-3}$	$+1.21 \cdot 10^{-2}$	$+2.22 \cdot 10^{-2}$	$+3.50 \cdot 10^{-2}$	$+5.04 \cdot 10^{-2}$	$+6.82 \cdot 10^{-2}$	$+8.84 \cdot 10^{-2}$	$+1.11 \cdot 10^{-1}$
40	$+2.19 \cdot 10^{-3}$	$+5.96 \cdot 10^{-3}$	$+1.16 \cdot 10^{-2}$	$+1.90 \cdot 10^{-2}$	$+2.83 \cdot 10^{-2}$	$+3.95 \cdot 10^{-2}$	$+5.25 \cdot 10^{-2}$	$+6.75 \cdot 10^{-2}$
45	$+1.22 \cdot 10^{-3}$	$+3.39 \cdot 10^{-3}$	$+6.65 \cdot 10^{-3}$	$+1.10 \cdot 10^{-2}$	$+1.64 \cdot 10^{-2}$	$+2.29 \cdot 10^{-2}$	$+3.05 \cdot 10^{-2}$	$+3.91 \cdot 10^{-2}$
50	$+7.92 \cdot 10^{-4}$	$+2.17 \cdot 10^{-3}$	$+4.17 \cdot 10^{-3}$	$+6.76 \cdot 10^{-3}$	$+9.87 \cdot 10^{-3}$	$+1.34 \cdot 10^{-2}$	$+1.74 \cdot 10^{-2}$	$+2.17 \cdot 10^{-2}$
55	$+5.41 \cdot 10^{-4}$	$+1.45 \cdot 10^{-3}$	$+2.75 \cdot 10^{-3}$	$+4.38 \cdot 10^{-3}$	$+6.30 \cdot 10^{-3}$	$+8.44 \cdot 10^{-3}$	$+1.08 \cdot 10^{-2}$	$+1.32 \cdot 10^{-2}$
60	$+3.14 \cdot 10^{-4}$	$+8.99 \cdot 10^{-4}$	$+1.81 \cdot 10^{-3}$	$+3.05 \cdot 10^{-3}$	$+4.65 \cdot 10^{-3}$	$+6.61 \cdot 10^{-3}$	$+8.95 \cdot 10^{-3}$	$+1.17 \cdot 10^{-2}$
65	$+5.32 \cdot 10^{-5}$	$+3.89 \cdot 10^{-4}$	$+1.12 \cdot 10^{-3}$	$+2.34 \cdot 10^{-3}$	$+4.13 \cdot 10^{-3}$	$+6.56 \cdot 10^{-3}$	$+9.70 \cdot 10^{-3}$	$+1.36 \cdot 10^{-2}$

cross sections, $\sigma^{\text{pp}} = |S_{\text{pp}}|^2$, are

$$\begin{bmatrix} \tilde{\sigma}^{\text{vv}} \\ \tilde{\sigma}^{\text{hh}} \end{bmatrix} = \begin{bmatrix} \sigma^{\text{vv}} + \sigma^{\text{vh}} T_{\text{hh}}^2 / T_{\text{vv}}^2 \\ \sigma^{\text{hh}} + \sigma^{\text{vh}} T_{\text{vv}}^2 / T_{\text{hh}}^2 \end{bmatrix}. \quad (31)$$

Note that the rotation of the radar relative to the horizontal plane may also impact the polarized measurements. If the radar is rotated clockwise by an angle, γ , versus the local horizontal, the scattering matrix in (26) is replaced by

$$\hat{\mathbf{S}} = \begin{bmatrix} \cos \gamma & \sin \gamma \\ -\sin \gamma & \cos \gamma \end{bmatrix} \begin{bmatrix} S_{\text{vv}} & S_{\text{vh}} \\ S_{\text{vh}} & S_{\text{hh}} \end{bmatrix} \begin{bmatrix} \cos \gamma & -\sin \gamma \\ \sin \gamma & \cos \gamma \end{bmatrix}. \quad (32)$$

However, the radar rotation is controlled with at least $\gamma \approx 1^\circ$ accuracy (actually better than that). Simple linear algebra shows that distortions due to the rotation are proportional to at least $\sin^2 \gamma \approx -35$ dB. This is less than typical polarization isolation for horns (-20 dB) and thus is not considered.

The CP contribution in (31) leads to the following relative systematic errors, $\delta(x) = (\tilde{x} - x)/x$, for the PP NRCS, $\sigma_{\text{pp}}^{\text{pp}}$, PD, $\Delta\sigma = \sigma_{\text{vv}}^{\text{vv}} - \sigma_{\text{hh}}^{\text{hh}}$, PR, $P = \sigma_{\text{vv}}^{\text{vv}} / \sigma_{\text{hh}}^{\text{hh}}$, and NP term:

$$\delta(\sigma_{\text{pp}}^{\text{pp}}) = \frac{\sigma_{\text{vh}}}{\sigma_{\text{vv}}^{\text{vv}}} \cdot \frac{T_{\text{hh}}^2}{T_{\text{vv}}^2} \quad (33)$$

$$\delta(\sigma_{\text{pp}}^{\text{hh}}) = \frac{\sigma_{\text{vh}}}{\sigma_{\text{hh}}^{\text{hh}}} \cdot \frac{T_{\text{vv}}^2}{T_{\text{hh}}^2} \quad (34)$$

$$\delta(\Delta\sigma) = \frac{\sigma_{\text{vh}}}{\Delta\sigma} \cdot \frac{|T_{\text{hh}}^4 - T_{\text{vv}}^4|}{T_{\text{vv}}^2 T_{\text{hh}}^2} \quad (35)$$

$$\delta(P) = \frac{1 + \delta(\sigma_{\text{vv}}^{\text{vv}})}{1 + \delta(\sigma_{\text{hh}}^{\text{hh}})} - 1 \approx \delta(\sigma_{\text{vv}}^{\text{vv}}) - \delta(\sigma_{\text{hh}}^{\text{hh}}) \quad (36)$$

$$\delta(\sigma_{\text{np}}) = \frac{\delta(\sigma_{\text{hh}}^{\text{hh}}) P_{\text{br}} - \delta(\sigma_{\text{vv}}^{\text{vv}}) P}{P_{\text{br}} - P}. \quad (37)$$

The first ‘‘scattering’’ factor in the RHS of (33)–(35) is the ratio between CP and PP (or their combination) and depends on the surface properties only. The second ‘‘antenna’’ factor is determined by the sensor properties and depends on the polarization isolation of transmitting antenna and how well its polarization plane is aligned with the 45° plane. The antenna distortion parameters T_{pp} are not calibrated separately, but the observations in Fig. 19(b) suggest that $(T_{\text{vv}}^2 R_{\text{vv}}^2) / (T_{\text{hh}}^2 R_{\text{hh}}^2) \approx 0.9$ or even closer to 1. Assuming that identical receiving channels have equal distortions, $R_{\text{vv}} \approx R_{\text{hh}}$, the transmit antenna distortions can be estimated as $T_{\text{vv}}^2 / T_{\text{hh}}^2 \approx 0.9$, and thus the antenna factor for the PD is ≈ 0.22 .

To evaluate the systematic errors in (33)–(37), we set all the antenna factors equal to 1, suggesting that the CP contaminates hybrid PP and PD, so that $\text{PP} = \text{PP} + \text{CP}$ and $\text{PD} = \text{PD} + \text{CP}$. Noting that $T_{\text{vv}}^2 / T_{\text{hh}}^2 \approx 0.9$ [indirectly confirmed by the data in Fig. 19(b)], this will give the upper limit of $\delta(\Delta\sigma)$ and reasonable estimates of δ for all other variables.

To the best of our knowledge, the CP empirical models are only available for the C-band [25], [45]. Therefore, in the absence of a better alternative, we assess the errors (33)–(37) using both the C-band CP GMF and TSM predictions. In accordance with the TSM, the ratio

TABLE III
COEFFICIENTS $A_j(\theta, U)$ FOR HH POLARIZATION

$\theta, ^\circ$	Wind speed U , m/s							
	3	5	7	9	11	13	15	17
A_0								
25	$+8.27 \cdot 10^{-2}$	$+1.46 \cdot 10^{-1}$	$+2.14 \cdot 10^{-1}$	$+2.84 \cdot 10^{-1}$	$+3.56 \cdot 10^{-1}$	$+4.31 \cdot 10^{-1}$	$+5.08 \cdot 10^{-1}$	$+5.86 \cdot 10^{-1}$
30	$+2.02 \cdot 10^{-2}$	$+4.39 \cdot 10^{-2}$	$+7.35 \cdot 10^{-2}$	$+1.08 \cdot 10^{-1}$	$+1.48 \cdot 10^{-1}$	$+1.92 \cdot 10^{-1}$	$+2.40 \cdot 10^{-1}$	$+2.92 \cdot 10^{-1}$
35	$+5.78 \cdot 10^{-3}$	$+1.49 \cdot 10^{-2}$	$+2.79 \cdot 10^{-2}$	$+4.47 \cdot 10^{-2}$	$+6.54 \cdot 10^{-2}$	$+8.98 \cdot 10^{-2}$	$+1.18 \cdot 10^{-1}$	$+1.50 \cdot 10^{-1}$
40	$+2.02 \cdot 10^{-3}$	$+5.88 \cdot 10^{-3}$	$+1.20 \cdot 10^{-2}$	$+2.04 \cdot 10^{-2}$	$+3.12 \cdot 10^{-2}$	$+4.46 \cdot 10^{-2}$	$+6.05 \cdot 10^{-2}$	$+7.91 \cdot 10^{-2}$
45	$+8.78 \cdot 10^{-4}$	$+2.75 \cdot 10^{-3}$	$+5.87 \cdot 10^{-3}$	$+1.03 \cdot 10^{-2}$	$+1.63 \cdot 10^{-2}$	$+2.37 \cdot 10^{-2}$	$+3.28 \cdot 10^{-2}$	$+4.36 \cdot 10^{-2}$
50	$+4.70 \cdot 10^{-4}$	$+1.52 \cdot 10^{-3}$	$+3.29 \cdot 10^{-3}$	$+5.88 \cdot 10^{-3}$	$+9.34 \cdot 10^{-3}$	$+1.37 \cdot 10^{-2}$	$+1.91 \cdot 10^{-2}$	$+2.56 \cdot 10^{-2}$
55	$+2.97 \cdot 10^{-4}$	$+9.59 \cdot 10^{-4}$	$+2.08 \cdot 10^{-3}$	$+3.71 \cdot 10^{-3}$	$+5.89 \cdot 10^{-3}$	$+8.67 \cdot 10^{-3}$	$+1.21 \cdot 10^{-2}$	$+1.61 \cdot 10^{-2}$
60	$+2.10 \cdot 10^{-4}$	$+6.69 \cdot 10^{-4}$	$+1.43 \cdot 10^{-3}$	$+2.54 \cdot 10^{-3}$	$+4.00 \cdot 10^{-3}$	$+5.84 \cdot 10^{-3}$	$+8.09 \cdot 10^{-3}$	$+1.08 \cdot 10^{-2}$
65	$+1.66 \cdot 10^{-4}$	$+4.96 \cdot 10^{-4}$	$+1.03 \cdot 10^{-3}$	$+1.79 \cdot 10^{-3}$	$+2.79 \cdot 10^{-3}$	$+4.04 \cdot 10^{-3}$	$+5.57 \cdot 10^{-3}$	$+7.37 \cdot 10^{-3}$
A_1								
25	$-9.70 \cdot 10^{-4}$	$-3.20 \cdot 10^{-3}$	$-6.21 \cdot 10^{-3}$	$-9.85 \cdot 10^{-3}$	$-1.40 \cdot 10^{-2}$	$-1.87 \cdot 10^{-2}$	$-2.38 \cdot 10^{-2}$	$-2.92 \cdot 10^{-2}$
30	$-3.40 \cdot 10^{-4}$	$+1.03 \cdot 10^{-3}$	$+3.89 \cdot 10^{-3}$	$+8.27 \cdot 10^{-3}$	$+1.42 \cdot 10^{-2}$	$+2.16 \cdot 10^{-2}$	$+3.05 \cdot 10^{-2}$	$+4.10 \cdot 10^{-2}$
35	$+4.75 \cdot 10^{-5}$	$+1.44 \cdot 10^{-3}$	$+4.47 \cdot 10^{-3}$	$+9.41 \cdot 10^{-3}$	$+1.64 \cdot 10^{-2}$	$+2.57 \cdot 10^{-2}$	$+3.74 \cdot 10^{-2}$	$+5.15 \cdot 10^{-2}$
40	$+1.62 \cdot 10^{-4}$	$+1.19 \cdot 10^{-3}$	$+3.42 \cdot 10^{-3}$	$+7.12 \cdot 10^{-3}$	$+1.25 \cdot 10^{-2}$	$+1.98 \cdot 10^{-2}$	$+2.92 \cdot 10^{-2}$	$+4.08 \cdot 10^{-2}$
45	$+1.89 \cdot 10^{-4}$	$+9.31 \cdot 10^{-4}$	$+2.45 \cdot 10^{-3}$	$+4.94 \cdot 10^{-3}$	$+8.53 \cdot 10^{-3}$	$+1.34 \cdot 10^{-2}$	$+1.96 \cdot 10^{-2}$	$+2.72 \cdot 10^{-2}$
50	$+1.94 \cdot 10^{-4}$	$+7.50 \cdot 10^{-4}$	$+1.79 \cdot 10^{-3}$	$+3.40 \cdot 10^{-3}$	$+5.66 \cdot 10^{-3}$	$+8.62 \cdot 10^{-3}$	$+1.24 \cdot 10^{-2}$	$+1.69 \cdot 10^{-2}$
55	$+1.90 \cdot 10^{-4}$	$+6.20 \cdot 10^{-4}$	$+1.35 \cdot 10^{-3}$	$+2.41 \cdot 10^{-3}$	$+3.82 \cdot 10^{-3}$	$+5.61 \cdot 10^{-3}$	$+7.80 \cdot 10^{-3}$	$+1.04 \cdot 10^{-2}$
60	$+1.68 \cdot 10^{-4}$	$+5.02 \cdot 10^{-4}$	$+1.03 \cdot 10^{-3}$	$+1.76 \cdot 10^{-3}$	$+2.69 \cdot 10^{-3}$	$+3.83 \cdot 10^{-3}$	$+5.19 \cdot 10^{-3}$	$+6.77 \cdot 10^{-3}$
65	$+1.20 \cdot 10^{-4}$	$+3.69 \cdot 10^{-4}$	$+7.65 \cdot 10^{-4}$	$+1.31 \cdot 10^{-3}$	$+2.01 \cdot 10^{-3}$	$+2.85 \cdot 10^{-3}$	$+3.83 \cdot 10^{-3}$	$+4.95 \cdot 10^{-3}$
A_2								
25	$+1.96 \cdot 10^{-2}$	$+4.52 \cdot 10^{-2}$	$+7.57 \cdot 10^{-2}$	$+1.10 \cdot 10^{-1}$	$+1.47 \cdot 10^{-1}$	$+1.87 \cdot 10^{-1}$	$+2.29 \cdot 10^{-1}$	$+2.74 \cdot 10^{-1}$
30	$+5.46 \cdot 10^{-3}$	$+1.61 \cdot 10^{-2}$	$+3.13 \cdot 10^{-2}$	$+5.07 \cdot 10^{-2}$	$+7.40 \cdot 10^{-2}$	$+1.01 \cdot 10^{-1}$	$+1.32 \cdot 10^{-1}$	$+1.65 \cdot 10^{-1}$
35	$+1.88 \cdot 10^{-3}$	$+6.16 \cdot 10^{-3}$	$+1.31 \cdot 10^{-2}$	$+2.28 \cdot 10^{-2}$	$+3.53 \cdot 10^{-2}$	$+5.07 \cdot 10^{-2}$	$+6.90 \cdot 10^{-2}$	$+9.02 \cdot 10^{-2}$
40	$+7.89 \cdot 10^{-4}$	$+2.64 \cdot 10^{-3}$	$+5.81 \cdot 10^{-3}$	$+1.05 \cdot 10^{-2}$	$+1.67 \cdot 10^{-2}$	$+2.46 \cdot 10^{-2}$	$+3.44 \cdot 10^{-2}$	$+4.60 \cdot 10^{-2}$
45	$+3.93 \cdot 10^{-4}$	$+1.27 \cdot 10^{-3}$	$+2.77 \cdot 10^{-3}$	$+4.97 \cdot 10^{-3}$	$+7.94 \cdot 10^{-3}$	$+1.17 \cdot 10^{-2}$	$+1.64 \cdot 10^{-2}$	$+2.20 \cdot 10^{-2}$
50	$+2.22 \cdot 10^{-4}$	$+6.76 \cdot 10^{-4}$	$+1.41 \cdot 10^{-3}$	$+2.44 \cdot 10^{-3}$	$+3.78 \cdot 10^{-3}$	$+5.45 \cdot 10^{-3}$	$+7.45 \cdot 10^{-3}$	$+9.80 \cdot 10^{-3}$
55	$+1.30 \cdot 10^{-4}$	$+3.69 \cdot 10^{-4}$	$+7.28 \cdot 10^{-4}$	$+1.20 \cdot 10^{-3}$	$+1.78 \cdot 10^{-3}$	$+2.45 \cdot 10^{-3}$	$+3.23 \cdot 10^{-3}$	$+4.08 \cdot 10^{-3}$
60	$+6.06 \cdot 10^{-5}$	$+1.74 \cdot 10^{-4}$	$+3.45 \cdot 10^{-4}$	$+5.76 \cdot 10^{-4}$	$+8.63 \cdot 10^{-4}$	$+1.21 \cdot 10^{-3}$	$+1.61 \cdot 10^{-3}$	$+2.06 \cdot 10^{-3}$
65	$-1.09 \cdot 10^{-5}$	$+1.84 \cdot 10^{-5}$	$+1.10 \cdot 10^{-4}$	$+2.87 \cdot 10^{-4}$	$+5.65 \cdot 10^{-4}$	$+9.63 \cdot 10^{-4}$	$+1.50 \cdot 10^{-3}$	$+2.18 \cdot 10^{-3}$

CP/PP reads [34], [41]

$$\frac{\sigma_{\circ}^{\text{vh}}}{\sigma_{\circ}^{\text{pp}}} = \frac{|G_{\text{vv}} - G_{\text{hh}}|^2}{|G_{\text{pp}}|^2} \frac{\overline{\zeta_c^2}}{\sin^2 \theta} \quad (38)$$

where G_{pp} are the Bragg scattering coefficients [34] and $\overline{\zeta_c^2}$ is the mean square slope of tilting wave in the plane normal to the incidence plane.

Calculations of the relative systematic errors δ are shown in Fig. 20 as omni-directional (azimuth-averaged) values versus incidence angle and wind speed. By definition, the TSM does not contain NP scattering, and therefore, no NP errors for the TSM are shown in Fig. 20.

The estimates based on the empirical data use a combination of PP C-band GMF [24] with different empirical C-band CP models from [25, Table 2a] and [45, Table II] and the estimate based on [24, Fig. 4]. Note that the substitution of the HH model [24] by that from [45, Table III] does not change the results significantly indicating that HH models from [24] and [45] are close.

In general, the TSM-based errors are below the empirical errors. Independent of particular data source, all empirical estimates of CP contamination of the measured PP and their derivatives (PR, PD, and NP) are small. Note also that the Ku-band airborne simultaneous PP and CP measurements [46, Fig. 7] at $U = 11$ m/s and $\theta = 44^\circ$ suggest the similarly low magnitude of δ comparable to that in the C-band. This suggests only a minor dependence on radar frequency that

allows using empirical C-band estimates as a proxy for our Ka-band.

The estimates shown in Fig. 20 suggest that the HH channel and the NP term are the most affected by CP contamination, for which up to 20% error is possible at large incidence angles. We tolerate such errors and ignore CP contribution to the hybrid measurements.

APPENDIX C EVALUATION OF (4)

At each iteration step, (4) is evaluated numerically for the given θ_0 , ϕ_0 , and U using the radar antenna pattern (Fig. 18). To improve computational performance, the integration in (4) is performed in $\{\alpha, \beta\}$ -coordinates (Fig. 21)

$$\sigma_{\circ\text{eff}}(\theta_0, \phi_0, U) = \frac{\int \Gamma_{\text{eff}} \sigma_{\circ}(\theta, \phi, U) J d\alpha d\beta}{\int \Gamma_{\text{eff}} J d\alpha d\beta}$$

$$\Gamma_{\text{eff}}(\alpha, \beta) = \Gamma(\alpha, \beta) \left[\frac{R_0}{R} \right]^4 = \Gamma(\alpha, \beta) \left[\frac{\cos \theta}{\cos \theta_0} \right]^4$$

$$\theta(\alpha, \beta) = \arctan \left\{ \left[\frac{\tan^2 \alpha}{\cos^2 \chi} + \tan^2 \chi \right]^{1/2} \right\}$$

$$\phi(\alpha, \beta) = \phi_0 + \arctan \left\{ \frac{\tan \alpha}{\cos \chi \tan \chi} \right\}$$

$$J(\alpha, \beta) = \frac{H^2}{\cos^3 \chi \cos^2 \alpha} \quad (39)$$

- [30] Royal Netherlands Meteorological Institute. *NSCAT-4 Geophysical Model Function*, accessed on Mar. 1, 2016. [Online]. Available: <http://projects.knmi.nl/>
- [31] V. N. Kudryavtsev, B. Chapron, A. G. Myasoedov, F. Collard, and J. A. Johannessen, "On dual co-polarized SAR measurements of the ocean surface," *IEEE Geosci. Remote Sens. Lett.*, vol. 10, no. 4, pp. 761–765, Jul. 2013.
- [32] W. J. Plant, "A two-scale model of short wind-generated waves and scatterometry," *J. Geophys. Res. Oceans*, vol. 91, no. C9, pp. 10735–10749, Sep. 1986.
- [33] V. Kudryavtsev, D. Hauser, G. Caudal, and B. Chapron, "A semi-empirical model of the normalized radar cross-section of the sea surface 1. Background model," *J. Geophys. Res. Oceans*, vol. 108, no. C3, pp. FET 2-1–FET 2-24, Mar. 2003, doi: 10.1029/2001JC001003.
- [34] G. R. Valenzuela, "Theories for the interaction of electromagnetic and ocean waves—A review," *Boundary-Layer Meteorol.*, vol. 13, no. 1, pp. 61–85, Jan. 1978.
- [35] T. Elfouhaily, D. R. Thompson, D. Vandemark, and B. Chapron, "A new bistatic model for electromagnetic scattering from perfectly conducting random surfaces," *Waves Random Media*, vol. 9, no. 3, pp. 281–294, 1999.
- [36] O. M. Phillips, *Dynamics of the Upper Ocean*. Cambridge, U.K.: Cambridge Univ. Press, 1977.
- [37] A. A. Mouche, D. Hauser, and V. Kudryavtsev, "Radar scattering of the ocean surface and sea-roughness properties: A combined analysis from dual-polarizations airborne radar observations and models in C-band," *J. Geophys. Res. Oceans*, vol. 111, no. C10, Sep. 2006, doi: 10.1029/2005JC003166.
- [38] M. V. Yurovskaya, V. A. Dulov, B. Chapron, and V. N. Kudryavtsev, "Directional short wind wave spectra derived from the sea surface photography," *J. Geophys. Res. Oceans*, vol. 118, no. 9, pp. 4380–4394, Sep. 2013.
- [39] N. J. M. Laxague, B. K. Haus, D. Bogucki, and T. Özgökmen, "Spectral characterization of fine-scale wind waves using shipboard optical polarimetry," *J. Geophys. Res. Oceans*, vol. 120, no. 4, pp. 3140–3156, Apr. 2015.
- [40] E. C. Monahan and D. K. Woolf, "Comments on 'Variations of whitecap coverage with wind stress and water temperature'," *J. Phys. Oceanogr.*, vol. 19, pp. 706–709, May 1989.
- [41] V. Kudryavtsev, I. Kozlov, B. Chapron, and J. A. Johannessen, "Quad-polarization SAR features of ocean currents," *J. Geophys. Res. Oceans*, vol. 119, no. 9, pp. 6046–6065, Sep. 2014, doi: 10.1002/2014JC010173.
- [42] B. Jähne and K. S. Riemer, "Two-dimensional wave number spectra of small-scale water surface waves," *J. Geophys. Res. Oceans*, vol. 95, no. C7, pp. 11531–11546, Jul. 1990.
- [43] S. R. Cloude and E. Pottier, "A review of target decomposition theorems in radar polarimetry," *IEEE Trans. Geosci. Remote Sens.*, vol. 34, no. 2, pp. 498–518, Mar. 1996.
- [44] J.-C. Souyris and S. Mingot, "Polarimetry based on one transmitting and two receiving polarizations: The $\pi/4$ mode," in *Proc. Int. Geosci. Remote Sens. Symp. (IGARSS)*, vol. 1, Jun. 2002, pp. 629–631.
- [45] J. W. Sapp, S. O. Alswiss, Z. Jelenak, P. S. Chang, S. J. Frasier, and J. Carswell, "Airborne co-polarization and cross-polarization observations of the ocean-surface NRCS at C-band," *IEEE Trans. Geosci. Remote Sens.*, vol. 54, no. 10, pp. 5975–5992, Oct. 2016.
- [46] S. H. Yueh, W. J. Wilson, and S. Dinardo, "Polarimetric radar remote sensing of ocean surface wind," *IEEE Trans. Geosci. Remote Sens.*, vol. 40, no. 4, pp. 793–800, Apr. 2002.



Yury Yu Yurovsky was born in Yalta, Russia, in 1984. He received the M.S. degree in geophysics from the Black Sea Branch, Moscow State University, Sevastopol, Ukraine, in 2006, and the Ph.D. degree in marine physics from the Marine Hydrophysical Institute (MHI), Sevastopol, Russia, in 2012.

Since 2007, he has been with MHI, where he is currently a Researcher, participating in activities at Black Sea Research platform. He is involved in obtaining and analysis of the data in various field experiments. His current research interests include ocean radar and optical remote sensing, sea surface dynamics, and air-sea interaction.



Vladimir N. Kudryavtsev received the Ph.D. and Senior Doctorate degrees in geophysics/marine physics from the Marine Hydrophysical Institute (MHI), Sevastopol, Russia, in 1981 and 1991, respectively.

In 1976, he joined MHI. From 2005 to 2013, he was with the Nansen Center, St. Petersburg, Russia. Since 2002, he has been a Professor with Russian State Hydro Meteorological University, St. Petersburg, where he is currently the Head of the Satellite Oceanography Laboratory. He is also a part-time Principal Scientist with MHI, and also holds a part-time Senior Position II with the Nansen Center, Bergen, Norway. His current research interests include air-sea interaction, atmospheric and oceanic boundary layers, and radar and optical imaging of the ocean surface.



Semyon A. Grodsky received the Ph.D. degree in geophysics from the Marine Hydrophysical Institute (MHI), Sevastopol, Russia, in 1986.

He joined MHI in 1999, and then joined the Atmospheric and Oceanic Science Department, University of Maryland at College Park, College Park, MD, USA, where he is currently a Senior Research Scientist. His current research interests include satellite remote sensing, air-sea interactions, and various aspects of ocean data analysis.



Bertrand Chapron was born in Paris, France, in 1962. He received the B.Eng. degree from the Institut National Polytechnique de Grenoble, Grenoble, France, in 1984, and the Doctorat National (Ph.D.) degree in fluid mechanics from the University of Aix-Marseille II, Marseille, France, in 1988.

He spent three years as a Post-Doctoral Research Associate at the NASA/GSFC/Wallops Flight Facility, Wallops Island, VA, USA. He has experience in applied mathematics, physical oceanography, electromagnetic waves theory, and its application to ocean remote sensing. He is currently responsible for the Oceanography from Space Laboratory, IFREMER, Plouzané, France.